

ALMA MATER STUDIORUM · UNIVERSITÀ DI BOLOGNA

Scuola di Scienze
Dipartimento di Fisica e Astronomia
Corso di Laurea Magistrale in Fisica

**Shoulder kinematic evaluation in patients
with rotator cuff tears using inertial and
magnetic sensors.**

Supervisor:
Prof. Nico Lanconelli

Co-supervisor:
Ing. Marco Muraccini

Submitted by:
Valentina Orsini

Accademic Year 2018/2019

Alla mia Famiglia,

A Marco

Abstract (IT)

La valutazione non invasiva della cinematica scapolo-toracica in relazione all'elevazione di omero svolge un ruolo centrale nell'analisi funzionale della spalla. All'interno del Centro Protesi INAIL é stato sviluppato un protocollo, chiamato *ISEO*, che ha come scopo l'analisi del ritmo scapolo-omerale. Tale protocollo si basa sull'utilizzo di sensori magneto-inerziali posizionati sul torace, sulla scapola, sull'omero e sull'avambraccio. L'accuratezza del protocollo ISEO é stata precedentemente analizzata in altri lavori, cosí come la sua affidabilitá intra- e inter-operatore [13][15]. Il protocollo ISEO é attualmente applicato nella valutazione dell'evoluzione del ritmo scapolo-omerale durante la riabilitazione di pazienti trattati chirurgicamente per lesione alla cuffia dei rotatori (patologia della spalla piú diffusa tra i lavoratori). Infatti, il ritmo scapolo-omerale (definito come il movimento coordinato tra scapola e omero, quando quest'ultimo é elevato) é uno dei parametri piú rilevanti dal punto di vista clinico. Questo progetto di tesi fa parte di un piú ampio studio clinico condotto all'interno dell'azienda NCS Lab (Carpi,(MO)), in collaborazione con il Dr. Claudio Chillemi (ICOT, Latina (RM)) che mira ad eseguire un confronto tra diverse tecniche chirurgiche per la riparazione della cuffia dei rotatori. Lo studio clinico in questione durerá circa due anni: per questo motivo i dati analizzati in questo progetto di tesi provengono solo dal gruppo di pazienti acquisiti nella fase preoperatoria. Tutti i dati sono stati acquisiti utilizzando i sensori magneto-inerziali *WISE* (tecnologia proprietaria dell'azienda NCS Lab). Questo lavoro di tesi si propone, quindi, di valutare la ripetibilitá del movimento in termini di coefficiente di correlazione multipla e di estrapolare alcuni parametri di interesse clinico come, ad esempio, i range di movimento (ROM) della scapola e dell'omero e il ritmo scapolo-omerale (SHR). Questi parametri sono stati poi caratterizzati da un punto di vista statistico al fine di valutare le differenze tra arto patologico e controlaterale. Sono state calcolate, inoltre, le prediction bands con lo scopo di

descrivere le differenze tra arto patologico e controlaterale nella coordinazione scapolo-omerale dei pazienti.

Per quanto riguarda la ripetibilità del movimento, i risultati ottenuti in questo lavoro di tesi mostrano che la rotazione medio-laterale é caratterizzata da un eccellente CMC sia per l'arto patologico che per il controlaterale. Inoltre, sono state riscontrate differenze significative dal punto di vista statistico tra le distribuzioni dei range di movimento dell'arto patologico e controlaterale. Tali differenze sono state trovate anche per quanto riguarda il ritmo scapolo-omerale.

Abstract (EN)

The non-invasive assessment of scapulo-thoracic kinematics, in relation to humerus elevation, plays a central role in the functional analysis of the shoulder. A protocol, named *ISEO* has been developed by INAIL Protheses Center in order to analyze the scapulo-humeral rhythm (SHR) in outpatient clinics, based on inertial and magnetic sensors positioned over the thorax, scapula, humerus and forearm. *ISEO* accuracy has been previously analyzed as well as its intra- and inter-operator reliability [13][15]. *ISEO* is currently applied to assess the evolution of the SHR during the rehabilitation of patients surgically treated for rotator cuff tear, which is the most diffused shoulder pathology among workers. In fact, the scapulo-humeral rhythm (defined as the coordinate movement between scapula and humerus, when the latter is elevated) is one of the clinical parameters heavily affected in most shoulder disorders.

This thesis project is part of a larger clinical study carried out within the NCS Lab company (Carpi,(MO)), in collaboration with Dr. Claudio Chillemi (ICOT Clinic, Latina (RM)). It aims to perform a comparison between different surgery techniques concerning the rotator cuff repair. The clinical study in question will last about two years and for this reason the data analyzed in this thesis project comes only from the group of patients acquired in the pre-operative stage. All data have been acquired using *WISE* inertial and magnetic sensors (proprietary technology of NCS Lab company). The aim of this thesis project was, therefore, to asses the repeatability of the movement in terms of the coefficient of multiple correlation and to extrapolate some parameters of clinical interest, that are the scapula and humerus ranges of movement (ROMs) and the scapulo-humeral rhythm (SHR). On these parameters a statistical characterization has been then performed in order to evaluate the differences between the pathological and contralateral upper limb. Moreover, based on the Gaussian theory, prediction bands have been computed in order to describe the contralateral-to-pathological side

differences in the scapulo-humeral coordination of patients.

With regard to the repeatability of the movement, the results obtained in this thesis work show that the medio-lateral rotation is characterized by an excellent CMC for both the pathological limb and the contralateral one. In addition, significant statistical differences were found between the ROMs distributions of the pathological and contralateral limb. These differences have also been found with regard to the scapulo-humeral rhythm.

Contents

Abstract (IT)	3
Abstract (EN)	5
1 Introduction	13
1.1 Clinical interest in shoulder kinematics	13
1.2 Inertial and magnetic sensors	18
1.2.1 Representation of orientation	21
1.2.2 Algorithms for orientation estimation	25
2 Materials and Methods	29
2.1 Wireless Inertial Sensor (<i>WISE</i>)	29
2.2 ISEO protocol	32
2.3 Rotator Cuff Repair protocol	36
2.4 Data processing	38
2.5 Coefficient of Multiple Correlation	39
2.6 Statistical tests for data analysis	41
2.7 <i>ROM</i> and <i>SHR</i>	45
2.8 Prediction bands	46
3 Results	49
3.1 Repeatability analysis	49
3.2 Range Of Motion	54
3.3 Scapulo-Humeral Rhythm	57
3.4 Prediction bands	60
4 Discussion and Conclusions	67

8

CONTENTS

Bibliography

71

List of Figures

1.1	Shoulder bones.	14
1.2	Muscles involved in shoulder flexion.	15
1.3	Muscles involved in shoulder abduction.	16
1.4	Scapula movements.	17
1.5	Example of a mass-spring-dampener system.	19
1.6	Operating system of a gyro.	20
1.7	Representation of the two coordinate systems.	22
1.8	Complementary filter.	26
2.1	WISE.	30
2.2	Gateway.	31
2.3	Elastic bands.	31
2.4	<i>SHoWlder</i> graphical interface.	32
2.5	Sensors positioning on the subject's thorax and scapula.	33
2.6	Sensors positioning on the subject's humerus and forearm.	33
2.7	Static calibration.	34
2.8	Rigid segments forming the upper limb.	35
2.9	Humerus flexion-extension and abduction-adduction.	35
2.10	Scapula PR-RE, ME-LA and P-A.	36
2.11	Visual description of step 1.	38
2.12	Visual description of step 3.	39
2.13	ME-LA vs. FL-EX angle-angle plots for different CMC values.	41
2.14	Representation of the three phases and of the linear regression performed on <i>I3</i>	46
3.1	CMC distributions in the sagittal plan of the contralateral side.	50
3.2	CMC distributions in the sagittal plan of the pathological side	50

3.3	CMC distributions in the frontal plan of the contralateral side. .	53
3.4	CMC distributions in the frontal plan of the pathological side .	53
3.5	ROMs distributions in sagittal and frontal plan.	55
3.6	ROMs distributions in the sagittal plan for each scapula rotation.	56
3.7	ROMs distributions in the frontal plan for each scapula rotation.	57
3.8	PR-RE SHR distributions for the first phase (<i>I1</i>) of humerus elevation and lowering in the sagittal plan.	58
3.9	ME-LA SHR distributions for the first phase (<i>I1</i>) of humerus elevation and lowering in the frontal plan.	60
3.10	Scapula PR-RE: comparison of contralateral and pathological PBs for the upward and downward phase of humerus elevation in the sagittal plan.	61
3.11	Scapula ME-LA: comparison of contralateral and pathological PBs for the upward and downward phase of humerus elevation in the sagittal plan.	62
3.12	Scapula P-A: comparison of contralateral and pathological PBs for the upward and downward phase of humerus elevation in the sagittal plan.	62
3.13	Scapula PR-RE: comparison of contralateral and pathological PBs for the upward and downward phase of humerus elevation in the frontal plan.	63
3.14	Scapula ME-LA: comparison of contralateral and pathological PBs for the upward and downward phase of humerus elevation in the frontal plan.	64
3.15	Scapula P-A: comparison of contralateral and pathological PBs for the upward and downward phase of humerus elevation in the frontal plan.	64

List of Tables

- 2.1 Technical specifications of WISE components. 31

- 3.1 CMC percentages for the contralateral limb in the sagittal plan. 51
- 3.2 CMC percentages for the pathological limb in the sagittal plan. 52
- 3.3 CMC percentages for the contralateral limb in the frontal plan. . 52
- 3.4 CMC percentages for the pathological limb in the frontal plan. . 54
- 3.5 Results of the Lilliefors test on the ROMs distributions. 56
- 3.6 Lilliefors test results (sagittal plan). 58
- 3.7 Results of the comparison between the SHR distributions of the
contralateral and pathological limb (sagittal plan). 59
- 3.8 Lilliefors test results (frontal plan). 59
- 3.9 Results of the comparison between the SHR distributions of the
contralateral and pathological limb (frontal plan). 61

Chapter 1

Introduction

In this first section a short excursus is proposed with respect to the clinical interest in shoulder kinematics and a new technology is presented that allows the motion analysis, i.e. inertial and magnetic sensors. In particular this thesis project will be focused on the upper limb kinematics.

1.1 Clinical interest in shoulder kinematics

The shoulder is a complex of joints of the upper limb and it is considered the most mobile of all the joints of the human body. It is characterized by three degrees of freedom (of movement) that allow the orientation of the upper limb in the three plans of space. These are defined by the three main anatomical axes: the transverse axis, the anterior-posterior axis and the longitudinal axis. Movements performed on the sagittal plane, around the transverse axis, are called flexion-extension, while those performed in the frontal plane (around the anterior-posterior axis) are referred to as adduction-abduction. As for the rotational movements (internal and external) of the arm, these occur around the longitudinal axis of the humerus. In particular the shoulder is defined as that complex of joints that allow the relative motion of the humerus respect to the thorax. The main bones that form the shoulder structure are: clavicle, humerus, scapula and thorax (Figure 1.1). These bones define five joints called: sternoclavicular (between sternum and clavicle), acromioclavicular (between scapula and clavicle), glenohumeral or scapulohumeral (between the glenoid fossa and the humerus), under-deltoid (between acromion and humerus) and scapulothoracic (between scapula and thorax). The first three joints are in anatomical

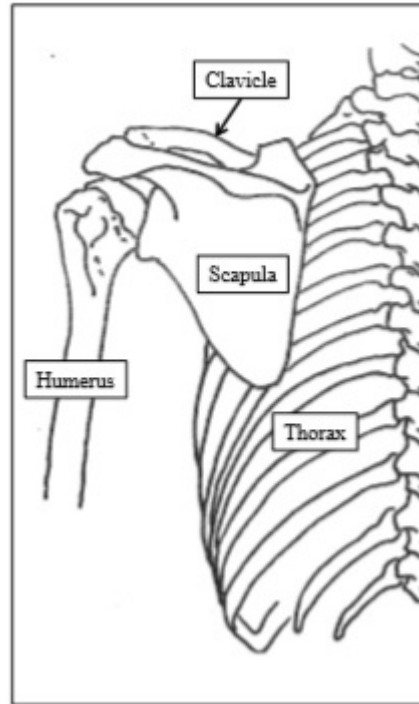


Figure 1.1: Shoulder bones.

sense, i.e. they consist of two surfaces covered by cartilage, while the last two consist of two surfaces which slide one with respect to the other without any interposed cartilage (i.e. are in the physiological sense)[1]. Among the five joints, the glenohumeral is one of the most complex articulation. This is due to the fact that it is able to cover a wide range of movement which, however, makes the structure vulnerable and prone to injuries. The stability of the joint is ensured by arm's and rotator cuff muscles, coraco-humeral and glenohumeral ligaments and the acromion and the subacromial bursa. All of these elements have the function of preventing from dislocations, keeping the humeral head in contact with the glenoid fossa during movements. In more detail, the rotator cuff is made up of a group of four muscles and tendons (supraspinatus, infraspinatus, teres minor and subscapularis), which stabilize the shoulder.

Moreover, it is possible to define the coordinated movement between scapula and humerus, when this latter is elevated, as the "scapulo-humeral rhythm" (SHR). Typically, the analysis of the SHR, from a clinical point of view, is conducted during the flexion and abduction movements of the humerus that occur respectively in the sagittal and in the frontal plane. Looking at the movement of the shoulder in these two planes, it emerges that $2/3$ of the movements (that

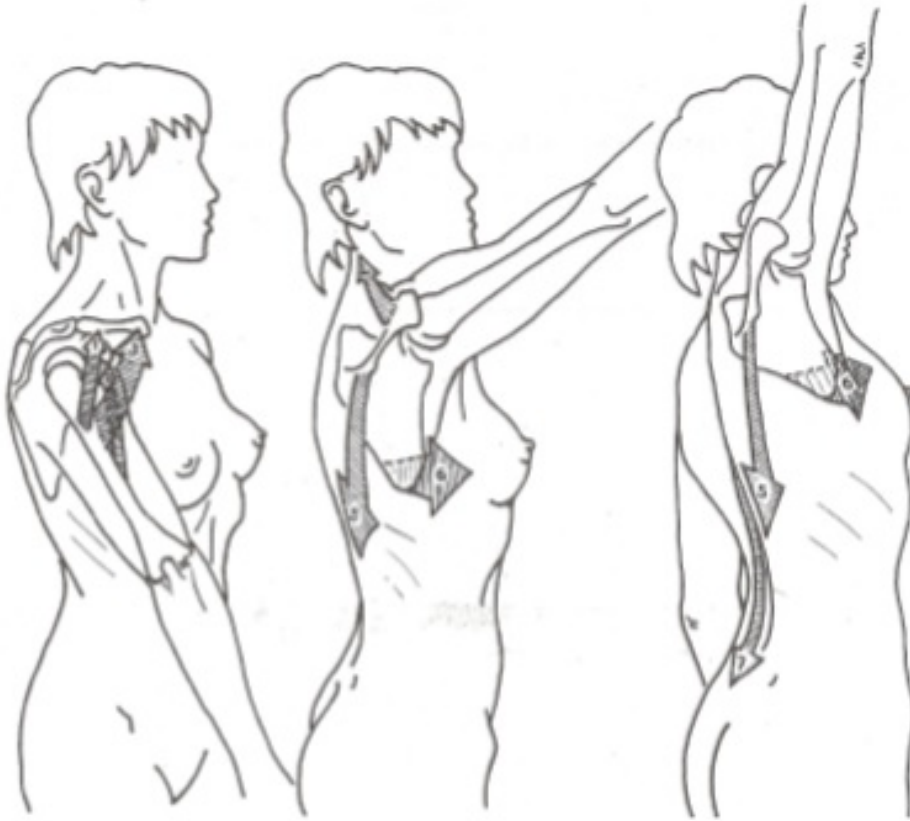


Figure 1.2: Muscles involved in shoulder flexion.

is 120°) is due to the glenohumeral mobility, while the remaining part is due to scapulothoracic mobility (that is 60°)[2],[3]. Based on the muscles involved, the flexion and abduction movements can therefore be divided into three phases. In particular, considering the flexion movement, it will be:

- from 0° to $50^\circ - 60^\circ$ anterior deltoid, coracobrachialis, greater pectoralis are recruited;
- from 60° to 120° the SHR starts and trapezius and latissimus dorsi are involved;
- from 120° to 180° the scapulo-thoracic and gleno-humeral movements interrupt and spinal muscles are activated.

As far as abduction is concerned, it follows that:

- from 0° to 90° deltoid and supraspinatus are recruited;

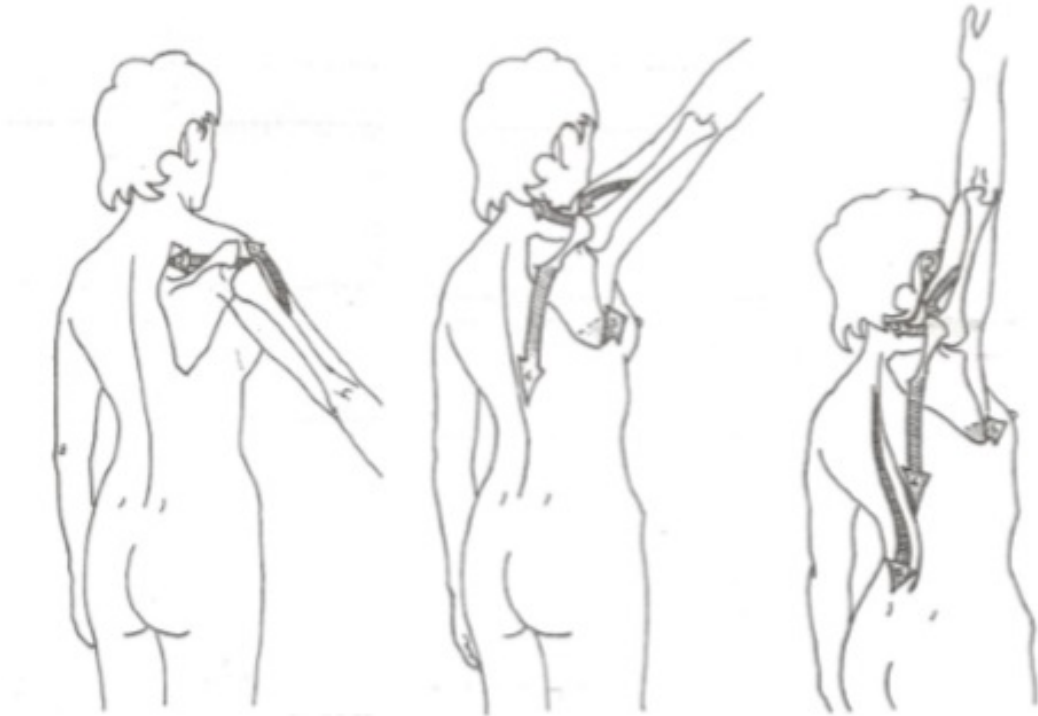


Figure 1.3: Muscles involved in shoulder abduction.

- from 90° to 150° the scapulo-humeral joint is blocked and the movement requires the involvement of the shoulder girdle (trapezius and latissimus dorsi);
- from 150° to 180° the spinal muscles are activated.

On the other hand, the scapula is described based on three additional rotation axes which define three different movements (Figure 1.4): medio-lateral rotation respect to the sagittal axis, anterior-posterior tilting around the transverse axis and internal-external rotation (or protaction-retraction) relative to the longitudinal axis. The balance between the structures that make up the shoulder can be altered as a result of traumatic events or degenerative pathologies that can lead to musculoskeletal diseases. Nowadays shoulder pathologies are an increasingly problem among workers and athletes. Some of the work-related factors associated with shoulder pain, which are shown in literature, are, for example, repetitive movements and forceful manual exertion. Research studies conducted with respect to this topic, report rotator cuff tear as the most common shoulder pathology and the main source of morbidity in working population [4],[5]: these

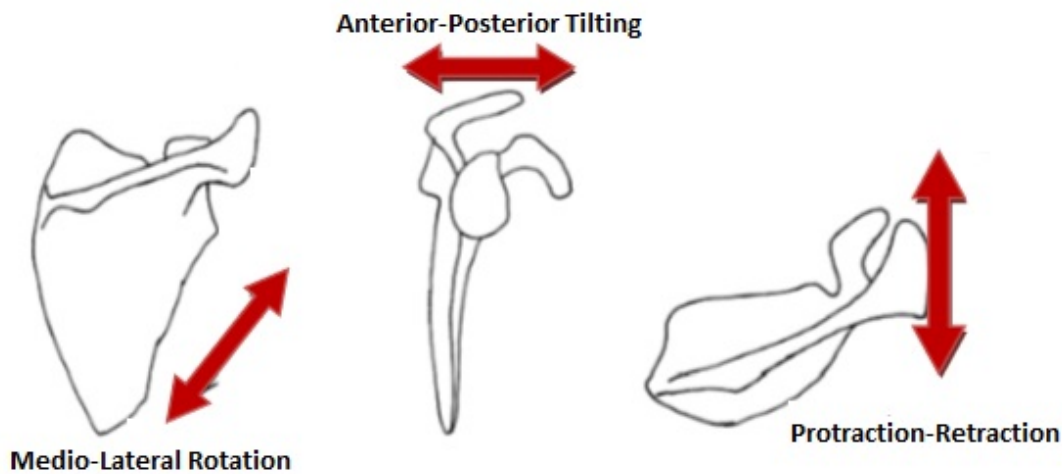


Figure 1.4: Scapula movements.

factors contribute to a high clinical interest in the study of shoulder kinematics. Moreover, a dysfunction of the rotator cuff anatomical structures can cause pain, joint weakness, lack of force and alterations in the scapula kinematics. In particular, this may result in changes in the scapulo-humeral rhythm. This alteration can be traced back to two main causes, namely protective factors or muscles dysfunctions[6],[7]. In the first case the subject uses adaptive movements to counteract perceived pain which lead to a reorganization in terms of muscle activity and scapula kinematics. With regard to muscles dysfunctions, these can be caused by a delay in the activation of a muscle or its inhibition and can contribute to the emergence of shoulder diseases. Shoulder pain, combined with upper limb dysfunctions, reduces the mobility of the joint and, therefore, the functional autonomy of the subject. The purpose of rehabilitative treatments is to recover the functionality of the upper limb and reduce pain in order to improve the patient's quality of life. Currently, in outpatient clinical settings, functional tests or clinical scales are used for patient evaluation. The most commonly used are, for example, the DASH questionnaire (Disabilities of the Arm, Shoulder and Hand), the Simple Shoulder Test (SST), the Constant-Murley test and the Visual Analogue Scale (VAS) for pain assessment and joint stiffness. Despite an easy execution, these tests and clinical scales do not allow an objective evaluation and are not able to provide sufficient information to specifically analyze the joint movement. Accurate in-vivo measurements (possibly in real-life conditions) are therefore necessary for a more thorough understanding of scapular

kinematics in relation to shoulder pathologies. The quantitative analysis of the SHR and of the cinematic features of the shoulder joint is a basic aspect for a complete evaluation of shoulder performance. It is also fundamental in order to make a diagnosis, to monitor the progress of a pathology, to check the result of a treatment or to plan a rehabilitation process. Unfortunately, these quantitative measures can only be carried out in a few highly advanced medical centres which are provided with motion analysis laboratories and expensive optoelectronic systems. Although these systems allow an accurate and non-invasive analysis of movement, they are very complex, hard to move and bulky to be placed in small clinics. Furthermore they are sensitive to external lighting sources and constrain kinematic analysis to a limited volume of space, preventing applicability for sports performance studies, home-care rehabilitation sessions or monitoring of daily activities. For these reasons, a new technology for motion analysis, based on inertial and magnetic measurements systems (IMMSs), has spread in recent years.

1.2 Inertial and magnetic sensors

Nowadays the accurate tracking of the orientation of rigid objects is critical in many application fields such as navigation of man-made vehicles, air and spacecrafts, robotics and ambulatory human movement analysis[8]. The latter includes a number of interesting applications, from monitoring of activities of daily living to virtual/augmented reality. Several technologies are available in order to develop motion tracking systems (trackers): one increasingly popular approach derive orientation estimates through the use of inertial and magnetic sensors. Contrary to other approaches, the one based on inertial and magnetic sensors does not require the presence of external sources (e.g. cameras for optical trackers, ultrasonic/electromagnetic transmitters for acoustic/electromagnetic trackers) that usually can operate only over relatively short distance in appropriate motion analysis laboratory. This advantage is due to the fact that they are able to measure physical quantities, such as linear acceleration and angular velocity, which are related to the motion of the objects where the sensors are fixed. Regarding magnetic sensing, it is based on an external reference, but the presence of a magnetic field on earth makes the magnetic source available everywhere. Recent technological progress have made it possible to obtain low cost

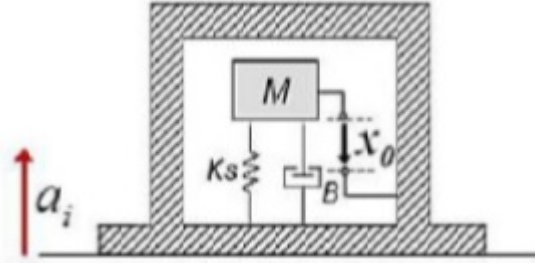


Figure 1.5: Example of a mass-spring-dampener system.

and highly miniaturized sensors (available to a wider market share) with good portability and wearables, that make the experimental set-up easier overall. For these reasons inertial/magnetic sensors can be considered an important tool for human subject motion analysis outside specialized laboratories.

Accurate estimates of three-dimensional orientation of a rigid body using these sensors require to take advantage from the properties of gyroscopes, accelerometers and magnetometers.

The accelerometer is able to convert linear acceleration into an electric magnitude and its functioning is based on a mass-spring-dampener system (Figure 1.5). The characteristic parameters of this system are, therefore, the inertial mass M (test mass), the elastic constant K_s , proper to the spring, and the damping factor B , linked to the damper. If x_0 represents the displacement of the mass relative to the *case* (supposedly fixed), follows that:

$$a_i = \ddot{x}_0 + \frac{B}{M}\dot{x}_0 + \frac{K_s}{M}x_0 \quad (1.1)$$

where a_i represents the acceleration to which the mass is subjected (external stress). The system is able to detect the movement of the mass thanks to the change in the electrical capacity of a capacitor depending on the distance between its armor: for this reason it is referred to as capacitive accelerometers. The first armor is made up of the mass M (of conductive material), while the second is attached to the structure of the device, near M . The capacity of this capacitor is detected by a circuit which also generates an electrical signal proportional to the position of the mass.

The gyroscope (Figure 1.6) is a rotating physical system whose function is to detect the speed at which the body rotates around a specific axis. Inertial gyroscopes typically consist of a vibrating mass, subject to the Coriolis force.

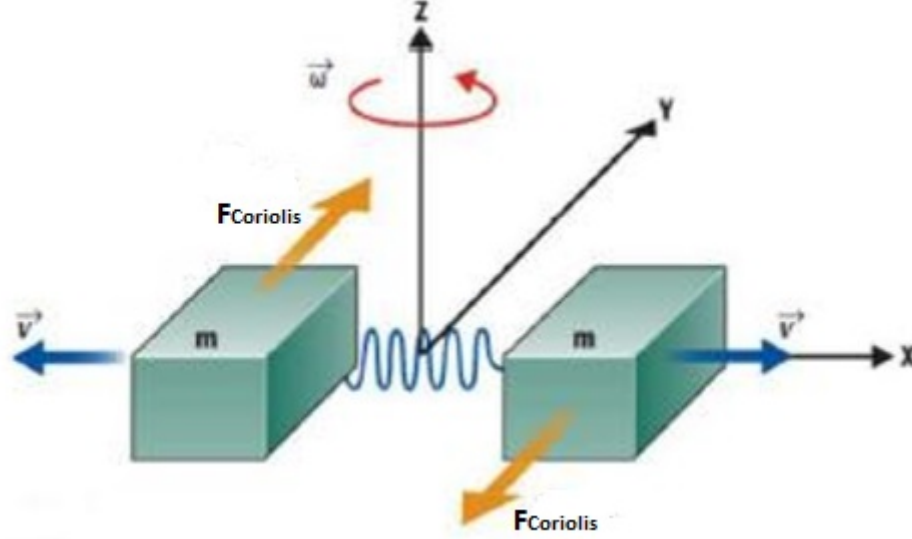


Figure 1.6: Operating system of a gyro.

Induced vibration can be detected through the use of capacitive, piezoresistive or piezoelectric mechanisms. The Coriolis acceleration is given by the following equation:

$$a_{cor} = 2v_x \times \omega_z \quad (1.2)$$

where v_x represents the rate at which the M mass moves (along the x -axis) due to the vibration imposed by an actuator, while ω_z is the angular velocity of the gyroscope along the z -axis. As mentioned above, the accelerometer is responsible for measuring acceleration in inertial devices. So, putting together equations (1.1) and (1.2) you get:

$$\ddot{x}_0 + \frac{B}{M}\dot{x}_0 + \frac{K_s}{M}x_0 = a_{cor} = 2v_x \times \omega_z \quad (1.3)$$

from which it is possible to derive ω_z .

The magnetometer is a device that can generate potential differences depending on the magnetic field it is subjected to: in the absence of external magnetic fields, it is able to measure the Earth's magnetic field vector, which can be considered constant within a medical clinic or motion analysis laboratory. There are different types of magnetometers, such as Hall effect sensors, magneto-resistors or induction sensors. Those based on the Hall effect represent the most versatile and highly sensitive technology. These magnetometers involve the use of conductive material that is immersed in a magnetic field. The potential difference is

directly proportional to the current intensity and to the magnetic field intensity and inversely proportional to the thickness of the crystal and the number of charges per unit of volume. As for magneto-resistors, on the other hand, these are made up of materials that change their resistivity according to the magnetic field to which they are subjected. However, they have a drawback related to the fact that they exhibit non-linear behaviour. Induction magnetometers, instead, consist of a coil that is moved in such a way as to properly modulate the magnetic flow within it. This technology is quite complex, cumbersome and is characterized by a low signal-to-noise ratio.

The orientation of a rigid body can therefore be computed by time-integrating the signals from a tri-axial gyroscopes, given the initial conditions. Although gyros can help achieving accurate orientation estimates, especially for highly dynamic motions, the signal results subject to errors due to low-frequency gyroscope bias drift. A tri-axial accelerometer allows to overcome these problems, providing drift-free inclinations estimates by sensing the gravity vector. It can be used together with a tri-axial magnetic sensor: this is called 'gyro-free aiding sensor system'. In this case, errors may be caused by the presence of nearby ferromagnetic materials that can critically disturb the signal. For these reasons sensor fusion techniques are necessary in order to achieve the best possible orientation estimates.

1.2.1 Representation of orientation

The orientation can be generally represented in three principal forms: Direction Cosine Matrix, Euler angles and quaternion[8]. Considering a rigid body, that's moving on or near the earth surface (at speed far below orbital velocity), it is possible to describe its orientation using two coordinate systems: the earth-fixed coordinate system and the body-fixed one. The first is an inertial coordinate system specified by the right-handed orthonormal basis $E = \{\mathbf{e}_1 \ \mathbf{e}_2 \ \mathbf{e}_3\}$, whose axes are directed in the local north, east and down directions. The body-fixed coordinate system is a non-inertial coordinate system specified by the right-handed orthonormal basis $B = \{\mathbf{e}'_1 \ \mathbf{e}'_2 \ \mathbf{e}'_3\}$. In the aeronautics jargon, its coordinate axes are named 'out the nose', 'out the right side' and 'out the belly' (Figure 1.7). An arbitrary vector \mathbf{x} can, then, be expressed in the

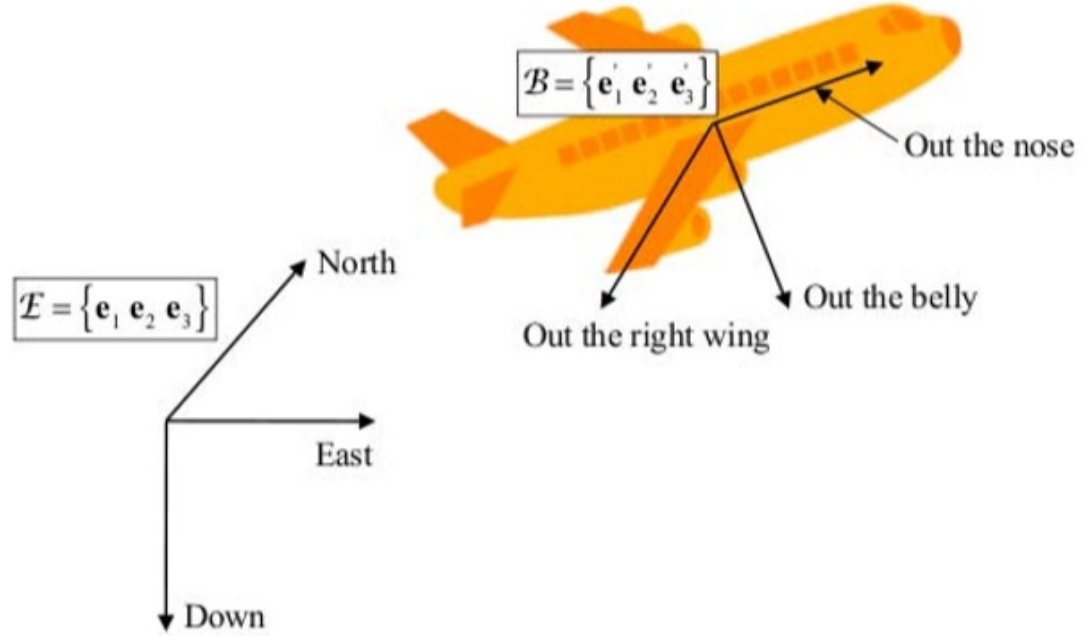


Figure 1.7: Representation of the two coordinate systems.

following equivalent forms:

$$\mathbf{x} = x_1\mathbf{e}_1 + x_2\mathbf{e}_2 + x_3\mathbf{e}_3 \quad (1.4)$$

$$\mathbf{x} = x'_1\mathbf{e}'_1 + x'_2\mathbf{e}'_2 + x'_3\mathbf{e}'_3 \quad (1.5)$$

It is also possible to represent the vector \mathbf{x} considering either basis, according to the relation:

$$\mathbf{x}_B = \mathbf{C}_E^B \mathbf{x}_E \quad (1.6)$$

where the indices B and E indicate which base is used for the vector representation and \mathbf{C}_E^B identifies the direction cosine matrix (DCM , also called orientation matrix). The columns of the DCM are the representation of the \mathbf{e}_i with respect to B while the rows are the representation of the \mathbf{e}'_i with respect to E (in both cases $i = 1, 2, 3$). This matrix is a 3×3 orthogonal matrix with unit determinant and belongs to the $SO(3)$, that is a $3D$ special orthogonal group of rotation matrices. From the orthogonality requirement it is possible to obtain a lower dimensional parameterization of the matrix, imposing six constraints on its nine elements. In particular, it is required that the column (row) vectors have a unit norm and that are mutually orthogonal. Therefore, the rotation matrix through an angle θ can be written, according to the Euler's formula, in the following two

equivalent expressions:

$$\begin{cases} \mathbf{R}(\mathbf{n}, \theta) = c_\theta \mathbf{I}_3 + (1 - c_\theta) \mathbf{n} \mathbf{n}^T - s_\theta [\mathbf{n} \times] \\ \mathbf{R}(\mathbf{n}, \theta) = \mathbf{I}_3 - s_\theta [\mathbf{n} \times] + (1 - c_\theta) [\mathbf{n} \times]^2 \end{cases} \quad (1.7)$$

\mathbf{I}_3 denotes the 3×3 identity matrix, \mathbf{n} denotes any unit column vector, c_θ and s_θ are compact notation for $\cos\theta$ and $\sin\theta$ respectively.

The orientation, in terms of the rotation vector, can also be expressed from the equation:

$$\boldsymbol{\theta} = \theta \mathbf{n} \quad (1.8)$$

In fact, according to the Euler's theorem, the motion of a rigid body with one point fixed is characterized by a rotation by an angle θ (i.e rotation angle $\in] - \pi, \pi[$) about some rotation axis \mathbf{n} . It is important to note that the rotation vector space does not contain singularity points.

The Euler angle formulation for the orientation is defined in terms of three consecutive rotation through three body-referenced Euler angles (i.e. ψ, θ, ϕ). So, the rotation matrix takes the following form:

$$\mathbf{R}(\psi, \theta, \phi) = \begin{bmatrix} c_\theta c_\psi & c_\theta s_\psi & -s_\theta \\ s_\phi s_\theta c_\psi - c_\phi s_\psi & s_\phi s_\theta s_\psi + c_\phi c_\psi & s_\phi c_\theta \\ c_\phi s_\theta c_\psi + s_\phi s_\psi & c_\phi s_\theta s_\psi - s_\phi c_\psi & c_\phi c_\theta \end{bmatrix} \quad (1.9)$$

This formulation is conceptually easy to understand, but may reach a singularity state commonly referred to as 'gimbal-lock'.

Finally, starting from Euler's formula (1.7) it is possible to derive another mathematical representation of the orientation matrix based on the Euler-Rodrigues symmetric parameters, aka quaternion:

$$\mathbf{R}(\mathbf{q}, q_4) = (q_4 - |\mathbf{q}|^2) \mathbf{I}_3 + 2\mathbf{q}\mathbf{q}^T - 2q_4[\mathbf{q} \times] \quad (1.10)$$

where

$$\mathbf{q} = \begin{bmatrix} q_1 \\ q_2 \\ q_3 \end{bmatrix} = \sin\left(\frac{\theta}{2}\right) \mathbf{n}, \quad q_4 = \cos\left(\frac{\theta}{2}\right) \quad (1.11)$$

Generally \mathbf{q} is called the vector part, while q_4 is the scalar part of the quaternion $\bar{\mathbf{q}} = [\mathbf{q}^T \quad q_4]^T$. Moreover, the rotation quaternion satisfies the normalization

constraint and it is possible to define the conjugate of a quaternion, its norm and inverse:

$$\bar{\mathbf{q}}^* = [-\mathbf{q}^T \ q_4]^T \quad (1.12)$$

$$|\bar{\mathbf{q}}| = \sqrt{\bar{\mathbf{q}}^* \otimes \bar{\mathbf{q}}} \quad (1.13)$$

$$\bar{\mathbf{q}}^{-1} = \frac{\bar{\mathbf{q}}^*}{|\bar{\mathbf{q}}|^2} \quad (1.14)$$

In the quaternion space two basic operations are defined: addition and multiplication. The first one is commutative, while the second one is not. If \mathbf{n} is an arbitrary unit vector, follows that a rotation about it is described by a unit quaternion (that is, quaternion with unit norm). The rule of composition of rotations is achieved by multiplying the corresponding quaternions:

$$\mathbf{R}(\bar{\mathbf{q}}) = \mathbf{R}(\bar{\mathbf{q}}_2)\mathbf{R}(\bar{\mathbf{q}}_1) \leftrightarrow \bar{\mathbf{q}} = \bar{\mathbf{q}}_2 \otimes \bar{\mathbf{q}}_1 \quad (1.15)$$

where $\bar{\mathbf{q}}_1$ and $\bar{\mathbf{q}}_2$ are arbitrary unit quaternion.

The advantage of using this representation is that it has the lowest dimension compared to any globally non-singular orientation parameterization. In addition, because $-\bar{\mathbf{q}}$ identifies the same rotation of $\bar{\mathbf{q}}$, the quaternion representation is redundant and a rotation through an angle θ about the \mathbf{n} -axis can be expressed as a rotation through an angle $-\theta$ about the $-\mathbf{n}$ -axis.

For both the *DCM* and the quaternion formulation, it is possible to determine the kinematic equations that describe the motion of a rigid body, computing the temporal derivative of the chosen orientation representation. As for the orientation matrix *DCM*, the motion is characterized by the Poisson's kinematic equations that represent a system of first-order linear differential equations:

$$\frac{d}{dt} \mathbf{C}_E^B = -[\boldsymbol{\omega}_B \times] \mathbf{C}_E^B \quad (1.16)$$

where $\boldsymbol{\omega}_B$ is the body-referenced angular velocity, defined as:

$$\boldsymbol{\omega}_B = \lim_{\delta t \rightarrow 0} \frac{\delta \boldsymbol{\theta}}{\delta t} \quad (1.17)$$

On the other hand, the time evolution of a quaternion, with angular velocity $\boldsymbol{\omega}_B$, is achieved by resolving the following first-order linear differential equation system:

$$\frac{d}{dt} \bar{\mathbf{q}} = \boldsymbol{\Omega}(\boldsymbol{\omega}_B) \bar{\mathbf{q}} \quad (1.18)$$

where $\mathbf{\Omega}(\boldsymbol{\omega}_B)$ is a 4×4 skew symmetric matrix.

The main advantages of using the quaternion parameterizations over the rotation matrix are related to errors associated with numerical integration of the kinematic equations and to the computational speed. In fact, quaternion representation is characterized by fewer numerical integration errors and does not require the computation of trigonometric functions.

1.2.2 Algorithms for orientation estimation

Data provided by body-fixed inertial/magnetic sensors are affected by noise and time-varying biases. Therefore, sensors-fusion algorithms are necessary to process the data and obtain a smooth and bias-free estimation of the orientation [8, 9].

There are mainly two different types of algorithms, proposed to solve the so-called Wahba's problem (originally introduced in 1965), that provide an estimate of the orientation: deterministic and stochastic. The first one is a least-squares approach that tries to minimize a least-square loss function. It consists in a constrained least-squared optimization problem whose goal is to find the rotation matrix from vector measurements taken at a single time. This single-frame method is connected with the operation of gyro-free aiding sensor systems and it is able to solve Wahba's problem without the need of an a priori estimate. The deterministic approach is based on the vector matching concept and, to work properly in human motion tracking, requires the measurements of constant reference vector that are gravity and earth magnetic field.

The stochastic approach (or Kalman filtering, first proposed in 1961) is based on the minimum-variance sequential estimates of orientation and of other parameters, such as sensor biases, using information obtained from motion dynamics. In other words, in order to produce the most accurate estimate of the system state, these algorithms use a model for predicting some aspects of a dynamic system and a model of the sensor measurements. The dynamic state is estimated using a Bayesian approach, which is based on propagating the probability density function (*PDF*) of the system state in a recursive manner through the application of the Bayes' rule:

$$p(\mathbf{x}_k | \mathbf{z}_{1:k}) \propto p(\mathbf{z}_k | \mathbf{x}_k) p(\mathbf{x}_k | \mathbf{z}_{1:k-1}) \quad (1.19)$$

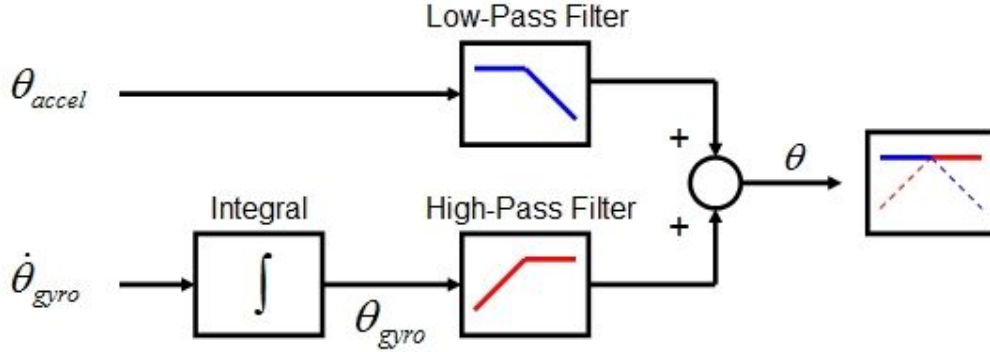


Figure 1.8: Complementary filter.

where $p(\mathbf{z}_k|\mathbf{x}_k)$ is the likelihood function defined by the measurement model as follow:

$$\mathbf{z}_k = h_k(\mathbf{x}_k, \mathbf{v}_k) \quad (1.20)$$

The term \mathbf{x}_k represents the system state and \mathbf{v}_k is the measurement noise whose statistics is known. Generally, h is a nonlinear time-variant function that performs a mapping of the state of the system to the measured state \mathbf{z}_k . Moreover, in (1.19), $p(\mathbf{x}_k|\mathbf{z}_{1:k-1})$ identifies the prior *PDF* of the state at time t_k . Kalman filtering based techniques model the state as a Gaussian distribution given the system's model. The knowledge of the $p(\mathbf{x}_k|\mathbf{z}_{1:k})$ (that is the posterior *PDF*) allows to estimate the state and to obtain measures of the accuracy of these estimates.

It is important to notice that both these sensor-fusion algorithms operate in the temporal domain, however, there are other approaches that operate in the frequency domain, that are complementary filters. These filters put together gyroscope data with acceleration and magnetic field measurements from sensors, in order to obtain an orientation estimation in quaternion form. A complementary filter performs high-pass filtering on the orientation estimated from gyroscope data affected by low-frequency noise. On the other hand, it performs a low-pass filter on accelerometer data affected by high-frequency noise: the fusion between the two estimations can ideally return an all-pass and noise-free orientation estimation (Figure 1.8).

The information obtained from the orientation of the body, therefore, allows to evaluate the joint kinematics: sensing units are placed on each body segment of interest and for each of them an anatomical reference system is defined. The

orientation of this latter is then expressed in the local sensor reference. According to standards set by the International Society of Biomechanics (ISB), joint kinematics can be obtained from knowledge of the relative orientation between two adjacent anatomical reference systems.

Chapter 2

Materials and Methods

In this chapter the technology used for data acquisitions on patients is shown and the protocol on which the upper limb kinematics analysis is based (*ISEO* protocol) is explained. Moreover, the protocol developed for the clinical study, of which this thesis project is part, and the methods used for data processing are presented. All data analyses were performed using MATLAB R2018a (The MathWorks, USA).

2.1 Wireless Inertial SEnsor (*WISE*)

Specific sensing units, aka *WISE* (proprietary technology of NCS Lab company, Carpi (MO)) were used in order to perform data acquisition. The *WISE* (Wireless Inertial SEnsor, Figure 2.1) is an inertial unit of measurement that incorporates 3D accelerometers, gyroscopes, and magnetometers (3D compass). The integrated processor manages the sampling, buffering, calibration and sensor-fusion algorithm of inertial and magnetic data, as well as the wireless network protocol for transmission. The sensor-fusion algorithm is an ad-hoc implemented algorithm which is part of the complementary filters. Combined with Netwis Manager software, real-time 3D orientation data can be obtained up to 10 wireless trackers. In addition, these sensors are able to provide linear acceleration, angular velocity and information related to the Earth's magnetic field. The radio protocol (which ensures synchronization of up to 10 devices over the wireless network) was specifically developed taking into account the inertial data of the sensor to ensure high accuracy of 3D motion tracking. The fact that this technology is completely wireless, allows to expand the possible application ar-



Figure 2.1: WISE.

eas and facilitates the wearability of the detection system, thus reducing set-up times. Moreover, since the sensors are not based on optical mechanisms and are therefore not influenced by lighting conditions, they can be used in various environments without the need of specific characteristics. Each *WISE* is $34.2\text{mm} \times 45.6\text{mm} \times 16.2\text{mm}$ and weighs 25g . The following hardware components are available within each device:

1. MEMS solid state accelerometer (*LIS344ALH*), with capacitive readout;
2. MEMS solid state gyroscope (*FXAS21002*), with capacitive readout;
3. magnetometer (*MMC3416xPJ*) made up of magneto-impedance sensor elements.

The datasheets ([10],[11],[12]) of the individual sensors included in the *WISE* provide the technical specifications that are summarized in Table 2.1.

WISE calculates orientation considering two reference systems: the first is a coordinate system fixed with the sensor, while the second is a earth fixed coordinate system. The latter is defined as follows: positive x-axis in magnetic local North direction, y-axis (in accordance with the right-hand rule) pointing West and positive z-axis pointing upwards. *WISE* output data, on the other hand, are described using quaternions in order to obtain the orientation representation. The accuracy with which these inertial sensors are able to estimate the orientation angle depends on how the data are acquired. In particular, for static acquisitions the error is less than 1° , while in the dynamic case the error is 2° .

	Angular velocity	Acceleration	Magnetic field
Dimension	3 axes	3 axes	3 axes
Full scale	2000°/s	6g	16G
Linearity	0.5% FSR	0.5% FSR	0.25% FSR
Bias stability	-	-	-
Noise	0.025 dps/ \sqrt{Hz}	50 μ g/ \sqrt{Hz}	1.5mG
Bandwidth	400Hz	1.8kHz	400Hz

Table 2.1: Technical specifications of WISE components.



Figure 2.2: Gateway.

To get better results using *WISE*, it is necessary to avoid highly magnetized areas when performing measurements. When the signal is distorted due to the proximity to a magnet or ferromagnetic material (iron or steel), the accuracy of the results can worsen. To work around this problem, it is possible to use the sensor-fusion algorithm to perform a check on the magnetic norm in the environment in which the measurements are performed.

The reception of synchronized data from all *WISE* is controlled through the use of the Gateway (Figure 2.2). This latter is able to receive wireless data up to a maximum of 10 *WISE*. To fix the sensors on the various anatomical districts of interest, elastic bands (equipped with Velcro) are available, that are able to adapt easily to the various anatomies (Figure 2.3). In addition, during the acquisition of data, the *SHoWlder* system, developed by NCS Lab, is used as



Figure 2.3: Elastic bands.

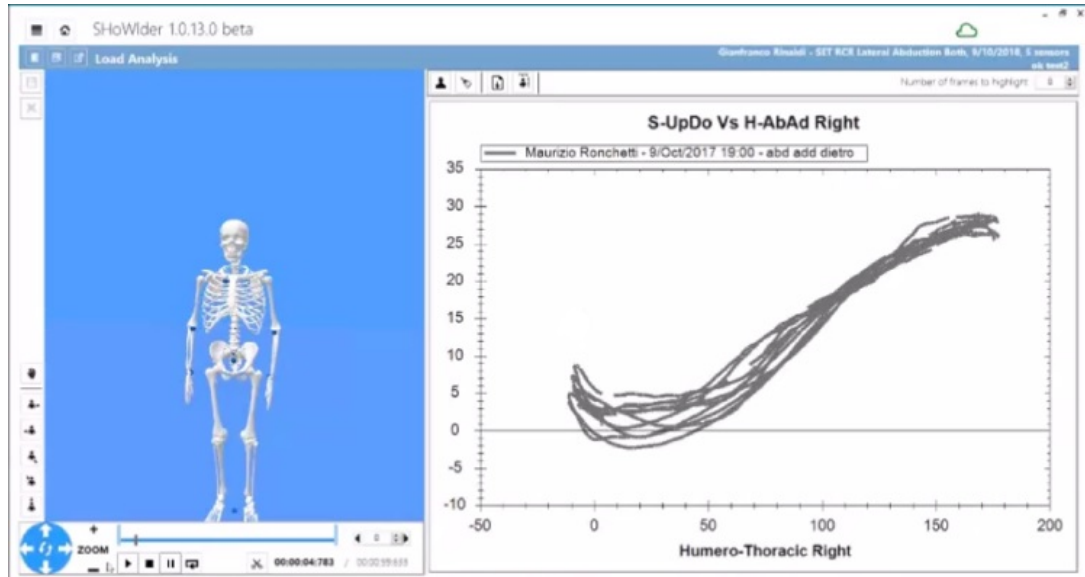


Figure 2.4: *SHoWlder* graphical interface.

software for data visualization and recording. This software was created within the *Showmotion* project, in order to objectively analyse the bio-mechanical behaviour of joints by pairing inertial technology with already validated protocols. This allows to see in real time (on the computer display) the variables of interest and the kinematic patterns (Figure 2.4). Using *SHoWlder* it is also possible to compare real-time analyses with those of previous tests, so as to monitor the evolution of a pathology, objectify the results of a surgical treatment and assess a patient's progress at various stages of rehabilitation.

2.2 ISEO protocol

ISEO (INAIL Shoulder & Elbow Outpatient-clinic protocol) is a motion analysis protocol, developed at INAIL Protheses Center (Bologna), that uses inertial and magnetic sensors to measure the upper limb 3D kinematics[13]. In particular, this protocol allows to measure scapulothoracic, humerothoracic and elbow kinematics in clinic. Scapulothoracic kinematics represents the major issue in evaluating shoulder pathologies. Moreover, the kinematic model developed in the protocol is based on functional and anatomical knowledge of the shoulder and elbow. The application of *ISEO* requires the following steps:

- sensors positioning on the subject's thorax, scapula, humerus and forearm.

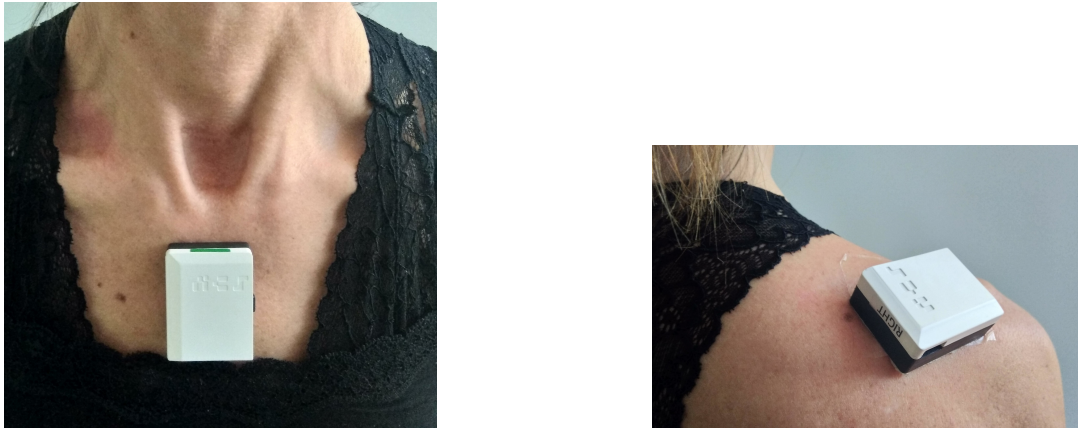


Figure 2.5: Sensors positioning on the subject's thorax and scapula.



Figure 2.6: Sensors positioning on the subject's humerus and forearm.

The thorax sensing unit is placed on the flat portion of the sternum, while the scapular one is placed just above the scapular spine (between the angulus acromialis and the trigonum spinae), aligning the sensor with the upper edge of the scapular spine (Figure 2.5). The humerus sensor is placed over the central third of the humerus, slightly posterior, in order to minimize the soft tissue artefact. Lastly, a sensing unit is positioned over the distal third of the forearm (Figure 2.6);

- defining the anatomical coordinate system, performing a static measure with the subject standing in a pre-defined posture (sensor-to-segment calibration). The subject will have to stand in the upright position, with the elbow flexed at 90° , in the neutral forearm rotation and with the humerus



Figure 2.7: Static calibration.

perpendicular to the ground in neutral rotation (Figure 2.7);

- defining the functional axes performing the so-called functional calibration. This latter is used in order to define the flexion-extension axis of the elbow and the pronation-supination axis of the forearm. Starting with the elbow flexed at 90° , in the neutral forearm rotation and with the humerus perpendicular to the ground in neutral rotation, the elbow flexion-extension movement and pronation-supination movement are executed;
- calculation of the joint kinematics. In particular, the kinematic model considered assumes the thorax, scapula, humerus and forearm to be rigid segments forming the upper limb (Figure 2.8). The orientations of the scapula and humerus are expressed relatively to the thorax, while the forearm orientation is computed with respect to the humerus. Scapulothoracic kinematics is characterized by three independent angles, that are: protraction-retraction ($PR - RE$), medio-lateral rotation ($ME - LA$) and anterior-posterior tilting ($AN - PO$). Concerning the humerus orientation, it is described in terms of flexion-extension ($FL - EX$), abduction-adduction ($AB - AD$) and internal-external rotation ($IN - EX$). The elbow is modeled with two hinge joints with non-intersecting axes and its kinematics is described by two independent angles: flexion-extension ($FL - EX$) and pronation-supination ($PR - SU$). Elbow kinematics is also characterized by a constant parameter, namely the carrying-angle, that measures the relative orientation of the axis of the hinges. It results

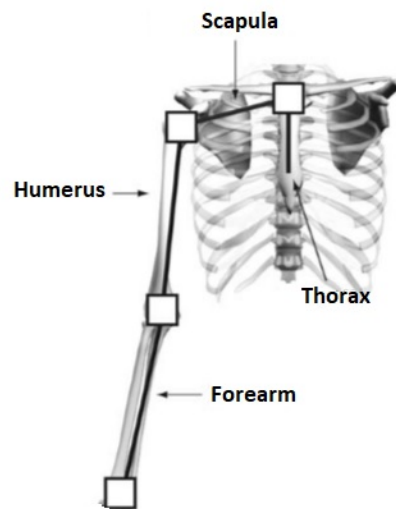


Figure 2.8: Rigid segments forming the upper limb.

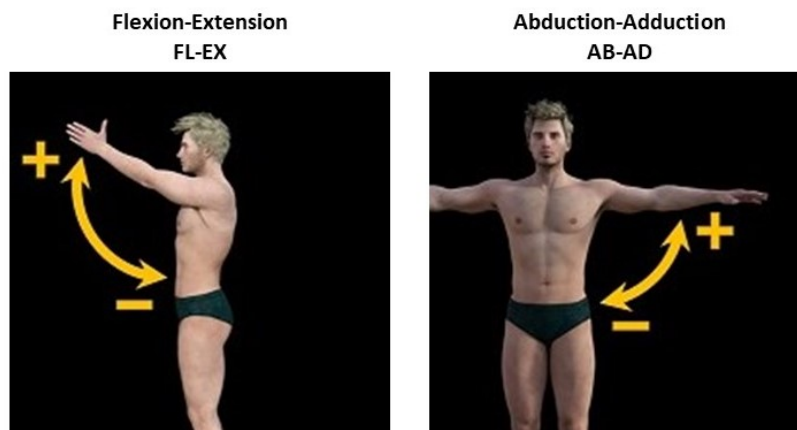


Figure 2.9: Humerus flexion-extension and abduction-adduction.

subject-specific and not necessarily null.

In this thesis project the three scapula rotations (PR-RE, ME-LA and P-A), with respect to the humerus flexion-extension and abduction-adduction, have been analyzed: a visual description of these movements is shown in Figure 2.9 and in Figure 2.10.

In addition, in this thesis project both the static and the functional calibration were performed through *SHoWlder*. This software (used for data visualization and recording) is provided with a function that allows to perform both calibrations in a few seconds, guiding the operator step-by-step: if an error occurs during this process, *SHoWlder* returns a warning message indicating that the

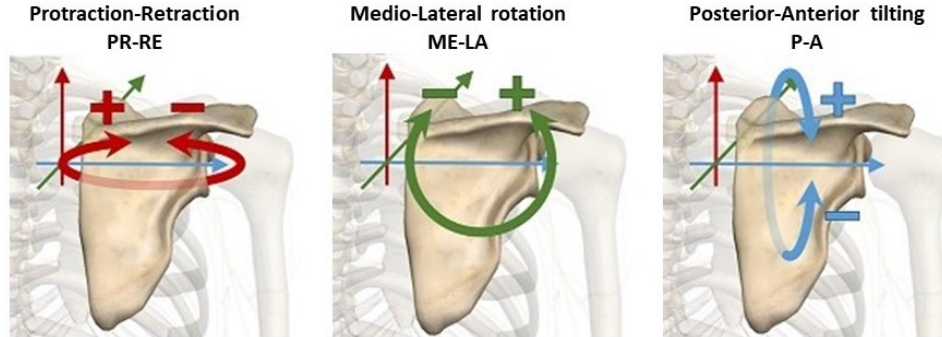


Figure 2.10: Scapula PR-RE, ME-LA and P-A.

calibration failed.

2.3 Rotator Cuff Repair protocol

The purpose of the clinical study, developed within NCS Lab company (Carpi (MO)), in collaboration with Dr. Claudio Chillemi (ICOT Clinic, Latina (RM)), is the comparison between different surgery techniques concerning the rotator cuff repair. The protocol proposed for the Rotator Cuff Repair analysis provides, as inclusion criteria, the involvement of patients with a diagnosis of full thickness rotator cuff tears and between the age of 18 and 75. Patients have also given their written informed consent to participate in the clinical study. On the other hand, the following have been identified as exclusion criteria: *SLAP* lesions, irreparable rotator cuff tear, glenohumeral arthrosis, neurologic disorders, age older than 75 or less than 18, active infections and the inability to participate in postoperative follow-up visits. Follow-up requires, in fact, the acquisition of data both in a pre-surgical phase and at three, six and twelve months after the operation.

The output evaluation consists in using NCS Lab inertial sensors in order to perform a kinematic analysis of shoulder during different movements, according to ISEO protocol. In particular, the different tasks identified are:

1. flexion-extension ($FL - EX$);
2. abduction-adduction ($AB - AD$);

3. internal-external rotation at 0° of $AB - AD$ ($I - E0$);
4. internal-external rotation at 90° of $AB - AD$ ($I - E90$);
5. exercise for evaluating the integrity of subscapularis (SUB).

Each analysis is performed at each follow-up in order to extrapolate the features of interest, i.e.: humerus range of motion (ROM) in $FL - EX$, $AB - AD$, $I - E0$, $I - E90$ and SUB , scapula protraction-retraction ($PR - RE$) ROM , scapula medio-lateral rotation ($ME - LA$) ROM , scapula anterior-posterior tilt ($A - P$) ROM and the scapulo-humeral rhythm (SHR).

The clinical study in question will last about two years and for this reason the data analyzed in this thesis project comes only from the group of patients acquired in the pre-operative stage. Going into detail, my thesis project has been divided into two phases: the acquisition phase and the data processing and analysis. As for the first, it was held at ICOT Clinic in Latina where 108 patients (age 62 ± 8) have been acquired using WISE inertial and magnetic sensors. During each acquisition session, the patients have been asked to perform two movements, i.e. humeral elevation in the sagittal plan (flexion-extension; FL-EX) and humeral elevation in the frontal plan (abduction-adduction; AB-AD). In particular, starting from a resting position, with the arms alongside the body, the patients were asked to elevate the humerus until maximum elevation (without pain) was reached and to return to the resting position. Each movement was repeated 7 times in a row, both in the sagittal and in the frontal plan. Moreover, the data have been acquired using *SHoWlder* system, developed by NCS Lab and both the pathological side and the contralateral one have been acquired at the same time.

The second phase has been carried on at NCS Lab company in Carpi, where the data have been processed and the following features of interest have been extrapolated: the humerus range of motion (ROM) in $FL - EX$ and $AB - AD$, the scapula protraction-retraction ROM , the scapula medio-lateral rotation ROM , the scapula anterior-posterior tilting ROM and the scapulo-humeral rhythm. A statistical analysis has been later performed. In the final step of the project the prediction bands have been calculated.

All the above concepts will be deepened in the following Sections.

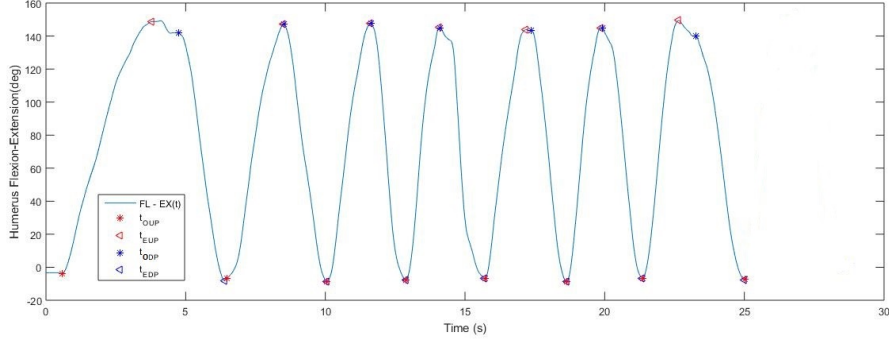


Figure 2.11: Visual description of step 1.

2.4 Data processing

Data acquired using *WISE* sensor-units are firstly pre-processed following the guidelines described in *ISEO* protocol [13]. These are then elaborated in such a way that each flexion-extension and abduction-adduction movement is divided into an upward and downward phase that can be representative of different kinematic patterns[14]. The algorithm on which data segmentation is based derives from the one suggested in [15] and consists mainly of three steps. In the first one, the following procedure is applied (Figure 2.11):

- selection of the local maxima and minima of the $FL - EX(t)$ curve;
- classification of points as the onset or the end of the upward phases (t_{OUP} and t_{EUP} respectively);
- the upward phases are checked in order to verify the presence of minima in the extracted curves. If this occurs, the curve is discarded, otherwise t_{OUP} and t_{EUP} are saved in a vector T ;
- classification of points as the onset or the end of the downward phases (t_{ODP} and t_{EDP} respectively);
- finally, the downward phases are checked in order to verify the presence of minima in the extracted curves. If this occurs, the curve is discarded, otherwise t_{ODP} and t_{EDP} are saved in a vector T .

Step 2 involves using T to segment $ME - LA(t)$, $PR - RE(t)$ and $P - A(t)$ in their upward and downward phases. In this way it is possible to obtain the

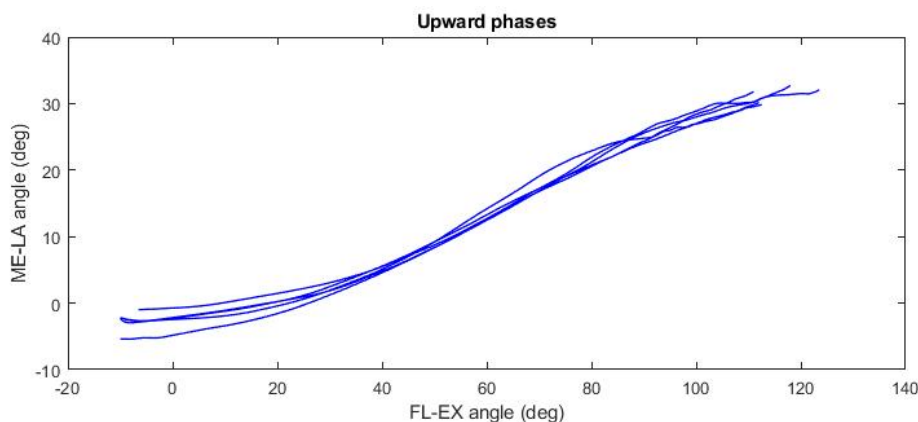


Figure 2.12: Visual description of step 3.

desired angle-angle plots, one for each phase, of $ME - LA$, $PR - RE$ and $P - A$ vs $FL - EX$. Lastly, in step 3 seven upward and downward phases are selected in order to obtain seven waveform for each plot: the first and last curve will then be discarded and not considered for further computations (Figure 2.12). The choice to discard the first waveform comes from the fact that generally, during the first repetition, patients have not yet become familiar with the movement they have to perform. The choice to discard the last waveform is based on the fact that patients, because of the pain, often don't carry out the movement.

The same steps are also applied for the segmentation of $AB - AD(t)$.

Following these steps, a total of 12 angle-angle plots are obtained, each containing 5 curves: 1)PR-RE vs. FL-EX, upward; 2)PR-RE vs. FL-EX, downward; 3)ME-LA vs. FL-EX, upward; 4)ME-LA vs. FL-EX, downward; 5)P-A vs. FL-EX, upward; 6)P-A vs. FL-EX, downward; 7)PR-RE vs. AB-AD, upward; 8)PR-RE vs. AB-AD, downward; 9)ME-LA vs. AB-AD, upward; 10)ME-LA vs. AB-AD, downward; 11)P-A vs. AB-AD, upward; 12)P-A vs. AB-AD, downward [15].

In order to carry out the data segmentation, in this thesis project an algorithm already implemented within NCS Lab company has been used.

2.5 Coefficient of Multiple Correlation

The repeatability of the movement, in the study of the upper limb kinematics, is a fundamental parameter that allows a quantitative analysis and a

consequent clinical use of the results. In describing the similarity or variability of waveforms, simple statistical methods do not yield satisfactory outcomes and are not descriptive of the variability between waveforms. In this study, a statistical measure, called the coefficient of multiple correlation (*CMC*), is used to describe the similarity between waveforms[16]. This coefficient enables repeatability assessment within a test day and is given by the following equation:

$$CMC = \sqrt{1 - \frac{\sum_{i=1}^M \sum_{j=1}^N \sum_{t=1}^T (Y_{ijt} - \bar{Y}_{it})^2 / MT(N-1)}{\sum_{i=1}^M \sum_{j=1}^N \sum_{t=1}^T (Y_{ijt} - \bar{Y}_i)^2 / M(NT-1)}} \quad (2.1)$$

where Y_{ijt} is the t th time point of the j th run on the i th test day. \bar{Y}_{it} is the average at time point t on the i th test day, given by:

$$\bar{Y}_{it} = \frac{1}{N} \sum_{j=1}^N Y_{ijt} \quad (2.2)$$

while \bar{Y}_i identifies the grand mean on the i th day:

$$\bar{Y}_i = \frac{1}{NT} \sum_{j=1}^N \sum_{t=1}^T Y_{ijt} \quad (2.3)$$

In equation (2.1), the numerator of the ratio represents the variance about the mean at time point t for a particular day, instead the denominator represents the total variability about the grand mean for the particular day. When the waveforms are similar, the numerator of the ratio tends to 0 and the *CMC* tends to 1. On the other hand, if the waveforms are dissimilar, both the numerator and denominator approximately represent the estimate of the same variance: in this case the ratio tends to 1 and *CMC* tends to 0.

For this study, the following intervals were identified for classifying the *CMC* obtained:

- $0.95 < CMC < 1$ excellent;
- $0.85 < CMC < 0.95$ very good;
- $0.75 < CMC < 0.85$ good;
- $0.65 < CMC < 0.75$ moderate;
- $0.55 < CMC < 0.65$ poor;

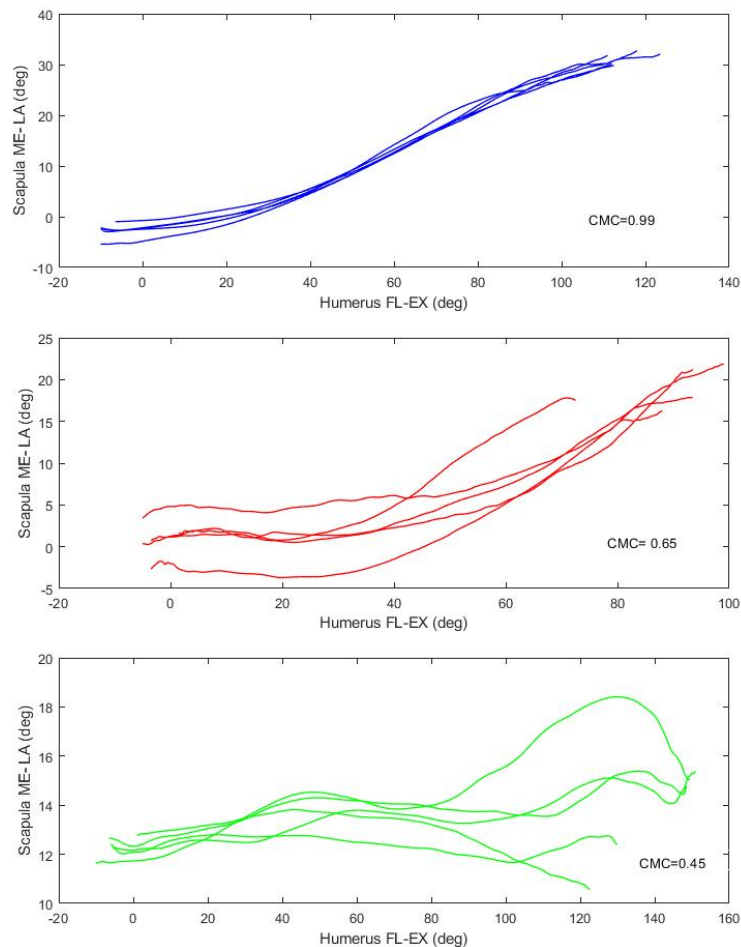


Figure 2.13: ME-LA vs. FL-EX angle-angle plots for different CMC values.

- $CMC < 0.55$ scarce.

In Figure 2.13 are shown three ME-LA vs. FL-EX angle-angle plots that correspond to three different CMC values, i.e. excellent, moderate and scarce respectively.

2.6 Statistical tests for data analysis

A common problem in statistical analysis is to decide whether several samples should be regarded as coming from the same population. Almost inevitably the samples differ, and the question is whether the differences signify differences among the populations, or are merely the chance variations to be expected

among random samples from the same population. In order to compare two or more data distributions, it is possible to use statistical tests, which, in general, are divided into two main categories: parametric and nonparametric tests. The first ones require prior knowledge about the distribution followed by the data or, equivalently, about the moments of the distribution. However there are cases where this knowledge is not available, and to overcome this situation it is necessary to apply nonparametric tests. These tests are also called distribution-free tests because they do not rely on information about the data underlying distribution. In fact, they order the observations according to their rank, that is, to array the N observations in order of magnitude and replace the smallest by 1, the next to smallest by 2, and so on, the largest being replaced by N . Not making assumptions about the population distribution is both an advantage and a disadvantage of such tests: their generality is certainly a strength of these nonparametric tests, however they do not exploit all the information contained in the data. Other important features of these tests are the quickness and ease of implementation and the fact that they are independent of any errors in the data distribution hypothesis[17, 18].

So, in general, these methods are used to test a given initial hypothesis (i.e H_0) about data distribution through the parameter α , that is the significance level (or α level) of the test. It represents the threshold value established for the test and together with the p – value determines whether or not the H_0 hypothesis is acceptable. The p – value denotes the probability of getting a result equal to or greater than an observed value, assuming that H_0 is true: it is called the observed significance value. If, for example, a null hypothesis H_0 and a threshold value ($\alpha=0.05$) are given, after calculating the p-value there are two possibilities:

1. $p \geq \alpha$, empirical evidence is not sufficiently contrary to the initial hypothesis and this cannot be rejected;
2. $p < \alpha$, empirical evidence is strongly opposed and therefore the null hypothesis should be rejected.

Typical significance values can be 0.05, 0.01 or 0.001 and depending on the choice it is possible to incur into different types of error. In particular, higher α -levels give less confidence about the result obtained and they risk rejecting a true H_0 . On the other hand, lower levels give more confidence about the result

but they may not reject a false hypothesis. It is, therefore, appropriate to make a compromise when choosing α threshold level.

The statistical tests used in order to perform data analysis in this thesis project are both parametric and nonparametric. In particular, the Lilliefors test is a normality test based on the Kolmogorov-Smirnov test and is suitable when the parameters of the null distribution are unknown and must be estimated. On the contrary, the Kolmogorov-Smirnov test requires the null distribution to be completely specified. The first step of the Lilliefors test consists in estimating of the population mean and population variance based on the data. Then, the maximum discrepancy between the empirical distribution function and the cumulative distribution function (*CDF*) of the normal distribution:

$$D = \max_x |\hat{F}(x) - G(x)| \quad (2.4)$$

$\hat{F}(x)$ represents the empirical *CDF* of the sample data, while $G(x)$ is the *CDF* of the hypothesized normal distribution with estimated parameters equal to the sample parameters. As in the Kolmogorov-Smirnov test, equation (2.4) identifies the test statistic. Finally, the last step consists of evaluating whether the maximum discrepancy is large enough to be statistically significant or not and in the first case the null hypothesis is rejected.

The conventional statistic for measuring the significance of a difference of means is termed *Student's t*. The latter is therefore a parametric test and is used when two distributions are thought to have the same variance, but possibly different means. Following the steps below it is possible to compute the *Student's t*. First of all, the standard error of the difference of the means is estimated from the pooled variance:

$$s_D = \sqrt{\frac{\sum_{i \in A} (x_i - \bar{x}_A)^2 + \sum_{i \in B} (x_i - \bar{x}_B)^2}{N_A + N_B - 2} \left(\frac{1}{N_A} + \frac{1}{N_B} \right)} \quad (2.5)$$

where each sum is over the points in one sample, the first or second, each mean likewise refers to one sample or the other. In addition N_A and N_B are the numbers of points in the first and second samples, respectively. The second step, instead, is to compute t by:

$$t = \frac{\bar{x}_A - \bar{x}_B}{s_D} \quad (2.6)$$

and finally the significance of this value of t for *Student's* distribution with $N_A + N_B - 2$ degrees of freedom is evaluated. The significance is a number

between zero and one, and represents the probability that $|t|$ could be this large or larger just by chance, for distributions with equal means. Therefore, a small numerical value of the significance (0.05 or 0.01) means that the observed difference is "very significant".

The Kruskal-Wallis test is a non-parametric method that is used in order to test whether samples originate from the same distribution. It represents a non-parametric version of classical one-way ANOVA, and an extension of the Wilcoxon (or Mann-Whitney U test) rank sum test for comparing more than two groups. Since it is a non-parametric method, this test does not assume a normal distribution of the data and it compares the medians of the groups to determine if the samples come from the same population or, equivalently, from different populations with the same distribution. The Kruskal-Wallis test is based on ranking data from all groups together (from smallest to largest) ignoring group membership. The rank for a tied observation is equal to the average rank of all observations tied with it. Then the test statistic is given by:

$$H = (N - 1) \frac{\sum_{i=1}^g n_i (\bar{r}_i - \bar{r})^2}{\sum_{i=1}^g \sum_{j=1}^{n_i} (r_{ij} - \bar{r})^2} \quad (2.7)$$

where n_i is the number of observations in group i , r_{ij} represents the the rank (among all observations) of observation j from group i and N is the total number of observations across all groups. Moreover, the average rank of all observations in group i , that is \bar{r}_i , and the average of all the r_{ij} (\bar{r}) are given by the following expressions:

$$\bar{r}_i = \frac{\sum_{j=1}^{n_i} r_{ij}}{n_i} \quad (2.8)$$

$$\bar{r} = \frac{1}{2}(N + 1) \quad (2.9)$$

Finally the test statistic (H) is compared to a critical value H_c obtained from a table for a given α - level: if H is bigger than H_c the null hypothesis is rejected. If ties are present, or the sample is big, the distribution of H can be approximated by a χ^2 distribution with $g - 1$ degrees of freedom.

The rank-sum test, which is also called the Wilcoxon, or Mann-Whitney, rank-sum test, is used to compare the means of two continuous distributions. When applied to the case of non-normal distributions, it is more powerful than the two-sample t-test discussed previously (Student's t test). The Mann-Whitney test is used to test the null hypothesis $H_0 : \mu_1 = \mu_2$ and proceeds following the

steps of the Kruskal-Wallis test. However, in this case the test statistic is given by:

$$u_{1,2} = w_{1,2} - \frac{n_{1,2}(n_{1,2} + 1)}{2} \quad (2.10)$$

where $w_{1,2}$ is the sums of rank numbers corresponding to the $n_{1,2}$ sets of observations.

2.7 ROM and SHR

The scapula Ranges Of Motion (ROMs) associated to the maximum ROM of humerus elevation are important parameters in evaluating the scapulo-humeral rhythm (SHR) in clinics [2] and it seems desirable to quantify them for each scapula rotation (PR-RE, ME-LA and P-A). For this reason, for each subject five ROMs of humeral flexion were identified, together with the correspondent scapula ROMs. The mean ROM over the five movement repetitions was then calculated both for humerus elevation and scapula rotations. These parameters have been extrapolated not only for the pathological upper limb, but also for the contralateral side, in order to verify the existence of statistically significant differences in the ROMs distribution related to the pathology.

Concerning the scapulo-humeral rhythm, it is defined as the coordinated movement between scapula and humerus, when this latter is elevated. From the clinical viewpoint, the SHR is mainly analyzed during humerus elevations in the sagittal, scapular and frontal plan. For each elevation plan, the SHR can be visualized by means of three angle-angle plots, whereby the scapulo-thoracic protraction retraction (PR-RE), the medio-lateral rotation (ME-LA) and the posterior-anterior tilting (P-A) are plotted against the humero-thoracic elevation [15].

In order to evaluate the SHR, in this study it was decided to proceed as described below, in accordance with the method proposed in [19] and [20].

First of all, for each patient the mean curve over the five movement repetitions was obtained for each angle-angle plot (specified in Section 2.4). Subsequently, it was decided to consider a humerus elevation (and lowering) range between 0° and 120° and this latter was divided into three equal phases, that are:

1. I_1 between 0° and 40° ;
2. I_2 between 40° and 80° ;

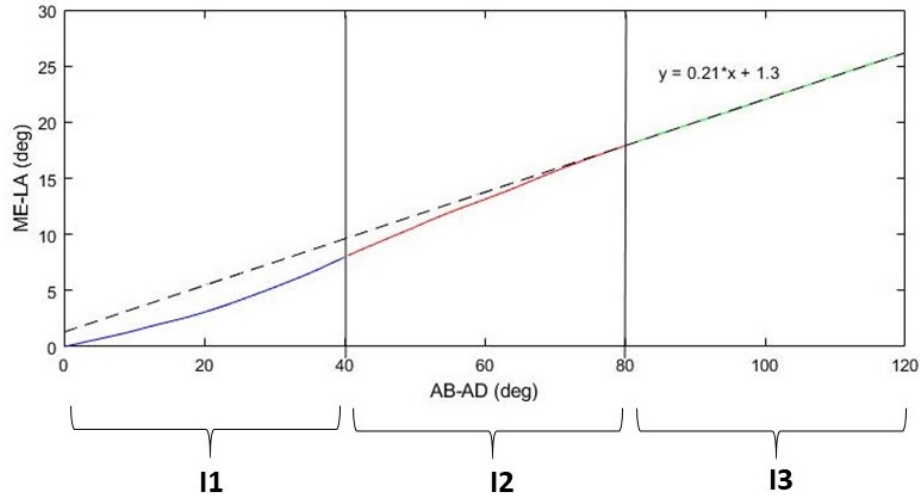


Figure 2.14: Representation of the three phases and of the linear regression performed on *I3*.

3. *I3* between 80° and 120°.

So, it was possible to perform a linear regression on each of the three segments and the slope of the line was associated with the SHR. In particular, Figure 2.14 shows an example of the three phases and of the linear regression (dotted line) performed on *I3*.

A statistical analysis was finally performed in order to investigate which of the three phases present significant differences between the pathological and contralateral limb. In fact, in the standard practice, *ISEO* protocol is applied to evaluate the evolution of the SHR during the rehabilitation of patients surgically treated for rotator cuff tears: in these subjects, the contralateral side is usually considered as reference after ensuring its anatomical and functional integrity [21]. The same investigations were performed for the abduction movement.

2.8 Prediction bands

The clinical application of *ISEO* protocol (see Section 2.2) would be facilitated via the availability of prediction bands that allow to measure the "distance" between the scapulo-humeral coordination of a new patient and that of controls subjects (that may be symptomatic or asymptomatic) [22]. In this

study the scapulo-humeral coordination of the patients was measured bilaterally and the prediction bands were computed in order to describe contralateral-to-pathological side differences.

For each subject the humerus elevation and lowering in the sagittal (FL-EX) and in the frontal (AB-AD) plan was measured together with the scapula protraction-retraction (PR-RE), medio-lateral rotation (ME-LA) and posterior-anterior tilting (P-A). As specified above, each patient was asked to repeat the movement seven times, but only the middle five were considered for calculations.

Starting from the 12 angle-angle plots (obtained following the method described in Section 2.4), a common range of humerus elevation was considered for all curves, from 0° to 120° . For each angle-angle plot, the mean curve from the five was then computed and the prediction bands were established through a parametric procedure based on the Gaussian theory and assuming a normal distribution [23]. In particular, the prediction bands were obtained by considering point-by-point intervals with amplitude of $1.96 \times \textit{standard error}$ (SE) either side of the mean curve calculated over all patients. The standard error of the sample mean depends on both the standard deviation (σ) and the sample size (N , that is equal to 108 in this study) by the relation:

$$SE = \frac{\sigma}{\sqrt{N}} \quad (2.11)$$

In fact, for a large sample, a 95% confidence interval is obtained as the values $1.96 \times SE$ either side of the mean.

Chapter 3

Results

3.1 Repeatability analysis

As mentioned above, in order to describe the similarity between waveforms (within a test day) the coefficient of multiple correlation (*CMC*) has been used [16].

Starting with the six angle-angle plots in the sagittal plan (i.e. PR-RE, ME-LA and P-A vs. FL-EX, upward and downward), six vectors have been obtained for the contralateral upper limb and six for the pathological one, each containing 108 CMC values (one for each patient involved in the analysis). On each vector, Lilliefors test was then performed in order to characterize the dataset and it has emerged that the values present in each vector do not follow a normal distribution ($p < 0.05$). For this reason, it was necessary to use the non-parametric Kruskal-Wallis test to verify whether the samples originate from the same distribution. From this test it has emerged that, both for the contralateral and the pathological side, significant statistical differences ($p < 0.01$) are present among the six CMC distributions. This result is highlighted in Figure 3.1 and in Figure 3.2 where the CMC distributions are represented through box plots.

Box plots provide a visual comparison of the CMC distributions: on each box, the central mark is the median, the edges of the box are the *25th* and *75th* percentiles (*1st* and *3rd* quantiles) and the whiskers extend to the most extreme data points that are not considered outliers. Outliers are plotted individually and are defined as values that are greater than the upper limit or less than the

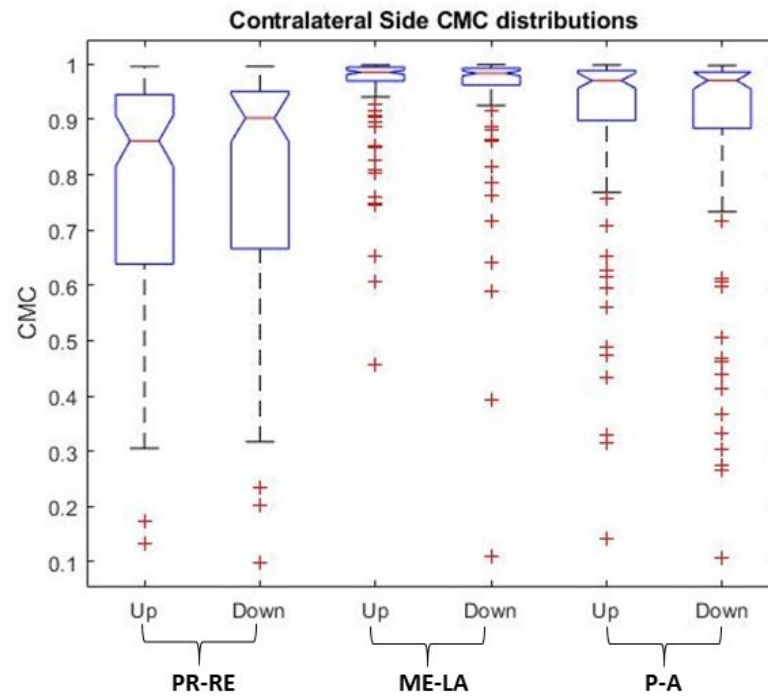


Figure 3.1: CMC distributions in the sagittal plan of the contralateral side.

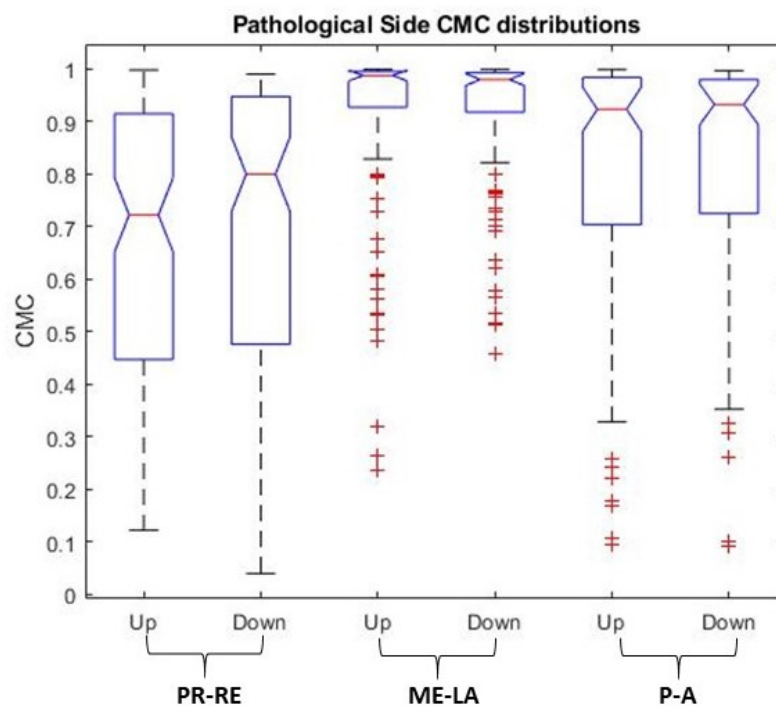


Figure 3.2: CMC distributions in the sagittal plan of the pathological side

CMC intervals (contralateral side)	PR-RE	ME-LA	P-A
$CMC > 0.95$	25%	82%	60%
$0.85 < CMC < 0.95$	30%	10%	22%
$0.75 < CMC < 0.85$	12%	4%	5%
$0.65 < CMC < 0.75$	8%	2%	2%
$0.55 < CMC < 0.65$	6%	1%	3%
$CMC < 0.55$	19%	1%	8%

Table 3.1: CMC percentages for the contralateral limb in the sagittal plan.

lower limit, defined as follows:

$$LowerLimit = q_1 - 1.5(q_3 - q_1) \quad UpperLimit = q_3 + 1.5(q_3 - q_1) \quad (3.1)$$

where q_1 and q_3 are the 25th and 75th percentiles, respectively. Moreover, the interval endpoints are the extremes of the notches and correspond to:

$$q_2 - \frac{1.57(q_3 - q_1)}{\sqrt{N}} \quad and \quad q_2 + \frac{1.57(q_3 - q_1)}{\sqrt{N}} \quad (3.2)$$

where q_2 is the median (50th percentile) and N is the number of observation. Looking at Figures 3.1 and 3.2, it is possible to note that the CMC distributions related to the ME-LA are the least spread compared to those related to the PR-RE and to the P-A. Moreover, it emerges that no significant differences are presents between the CMC distributions of the PR-RE upward and downward phases for the contralateral side. The same results were obtained for the pathological side and for the ME-LA and P-A upward and downward phases. For this reason, the upward phase and downward phase were considered together in the calculation of CMC percentages. These latter are shown in Table 3.1 and in Table 3.2 and were calculated considering a total of 216 CMC values.

The tables show that the medio-lateral rotation in the sagittal plan is characterized by an excellent CMC both for the contralateral and pathological side: in fact, it results > 0.95 in 82% and in 70% of cases respectively. It is possible to note, however, lower percentages for both the protraction-retraction and the posterior-anterior tilting. This could be due to either an instrumental factor or a factor related to the pathology of patients analyzed. As for the first case, it is known that the protraction-retraction angles are the ones that the sensors estimate with more difficulty and this could be reflected in a less accurate acquisition of the joint movement, resulting in a lower CMC. On the other hand,

CMC intervals (pathological side)	PR-RE	ME-LA	P-A
$CMC > 0.95$	21%	70%	44%
$0.85 < CMC < 0.95$	19%	11%	20%
$0.75 < CMC < 0.85$	12%	6%	8%
$0.65 < CMC < 0.75$	11%	4%	8%
$0.55 < CMC < 0.65$	5%	4%	3%
$CMC < 0.55$	32%	5%	17%

Table 3.2: CMC percentages for the pathological limb in the sagittal plan.

CMC intervals (contralateral side)	PR-RE	ME-LA	P-A
$CMC > 0.95$	28%	80%	55%
$0.85 < CMC < 0.95$	29%	10%	23%
$0.75 < CMC < 0.85$	12%	4%	7%
$0.65 < CMC < 0.75$	6%	2%	3%
$0.55 < CMC < 0.65$	6%	1%	3%
$CMC < 0.55$	19%	3%	9%

Table 3.3: CMC percentages for the contralateral limb in the frontal plan.

in this thesis project are involved patients with a diagnosis of full thickness rotator cuff tears at a pre-operative stage: the presence of pain and compensatory movements (which also affect the contralateral side) could play a key role in the repeatability of the movement. Despite the fact that some patients have a very low CMC (even less than 0.55) it was chosen not to discard them and to include them anyway in the analyses presented in the following sections.

Concerning the analyses in the frontal plan (abduction-adduction), it is possible to derive the same conclusions discussed previously. In particular, the CMC distributions are represented through box plots in Figure 3.3 and in Figure 3.4.

Moreover, in Tables 3.3 and 3.4 the CMC percentages, obtained for both the contralateral and the pathological limb, are shown. Again, the upward and downward phase have been considered together for the percentages calculation.

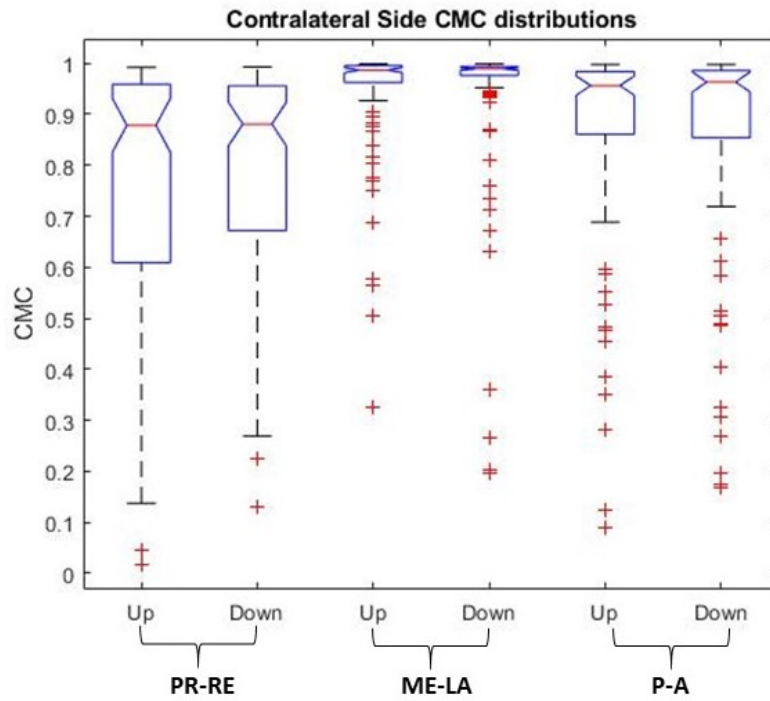


Figure 3.3: CMC distributions in the frontal plan of the contralateral side.

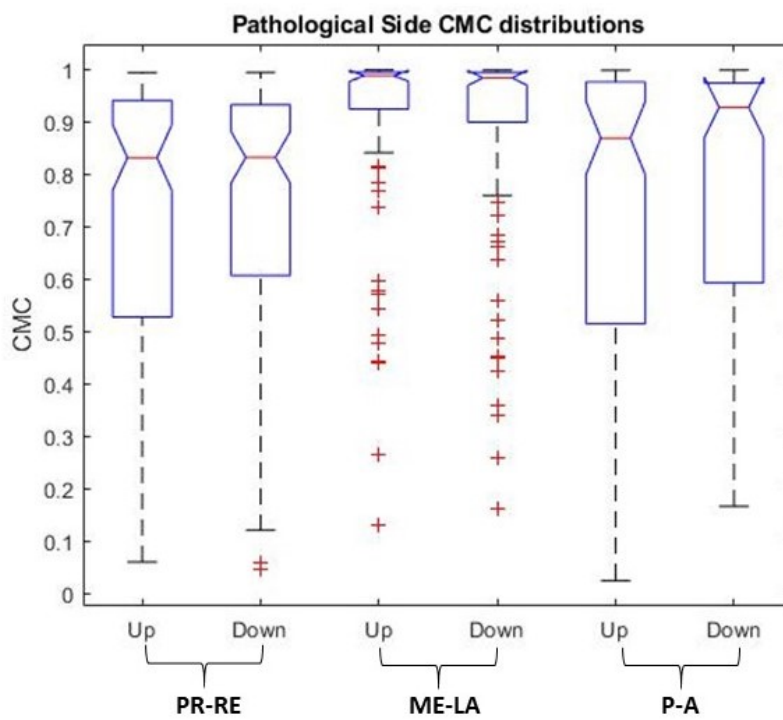


Figure 3.4: CMC distributions in the frontal plan of the pathological side

CMC intervals (pathological side)	PR-RE	ME-LA	P-A
$CMC > 0.95$	18%	69%	37%
$0.85 < CMC < 0.95$	28%	14%	20%
$0.75 < CMC < 0.85$	15%	5%	8%
$0.65 < CMC < 0.75$	8%	3%	6%
$0.55 < CMC < 0.65$	6%	2%	4%
$CMC < 0.55$	25%	7%	25%

Table 3.4: CMC percentages for the pathological limb in the frontal plan.

3.2 Range Of Motion

Humerus ROM

Firstly, the humerus elevation mean ROMs, both on the sagittal and frontal plan, have been analysed in order to verify the existence of statistically significant differences in their distribution related to the pathology.

The Lilliefors test highlighted that only the ROMs in FL-EX for the contralateral limb were normally distributed ($p = 0.5$), so it was decided to proceed applying the Mann-Whitney rank sum test for comparing two groups (that are, contralateral and pathological ROMs distributions). It has emerged that both for the sagittal and the frontal plan, the humerus ROMs for the pathological and contralateral side do not originate from the same distribution ($p < 0.05$). This can be observed in Figure 3.5 where the ROMs distributions are represented through box plots.

Looking at Figure 3.5, it is also possible to note that the ROMs distributions of the pathological sides are more spread compared to those of the contralateral sides. In addition, the ROMs median values of the pathological limb are smaller than those of the contralateral limb for both FL-EX and AB-AD.

Scapula ROMs

After the humerus elevation mean ROMs, the scapula mean ranges of motion have been taken into account.

The Lilliefors test was performed on the ROMs distribution for each scapula rotation (PR-RE, ME-LA and P-A) in the sagittal plan: the two groups related to

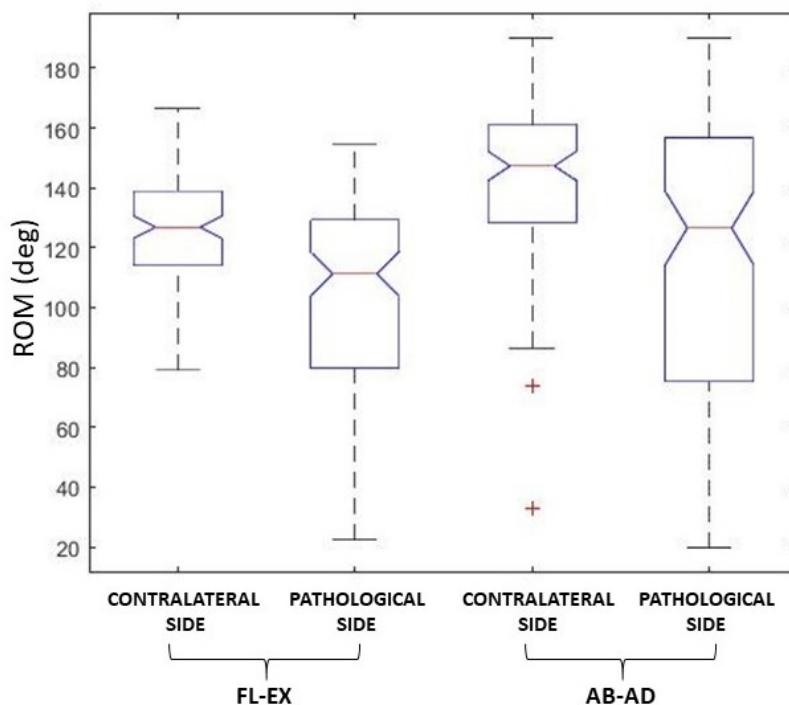


Figure 3.5: ROMs distributions in sagittal and frontal plan.

the scapula medio-lateral rotation have turned out to be normally distributed ($p = 0.2$ and $p = 0.5$ for the contralateral side and pathological side respectively), while the null hypothesis of the test was rejected for the other four groups examined ($p < 0.05$). For this reason, it was chosen to proceed applying the Mann-Whitney test to compare the pathological and contralateral ROMs distributions for the protraction-retraction and posterior-anterior tilting. It has emerged that, in both scapula rotations, statistically significant differences ($p < 0.05$) are present between the ROMs distributions of the pathological side (P-SIDE) and of the contralateral side (C-SIDE). On the other hand, the two ME-LA ROMs distributions were compared performing the Student's t test: in this case, no statistically significant differences ($p = 0.4$) were found for the two samples groups.

In Figure 3.6 the box plots of ROMs distributions in the sagittal plan (for each scapula rotation) are represented. Considering PR-RE and P-A, it is possible to note that the ROMs median values of the pathological limb are smaller than those of the contralateral limb.

The same analysis was carried out for each scapula rotation in the frontal plan

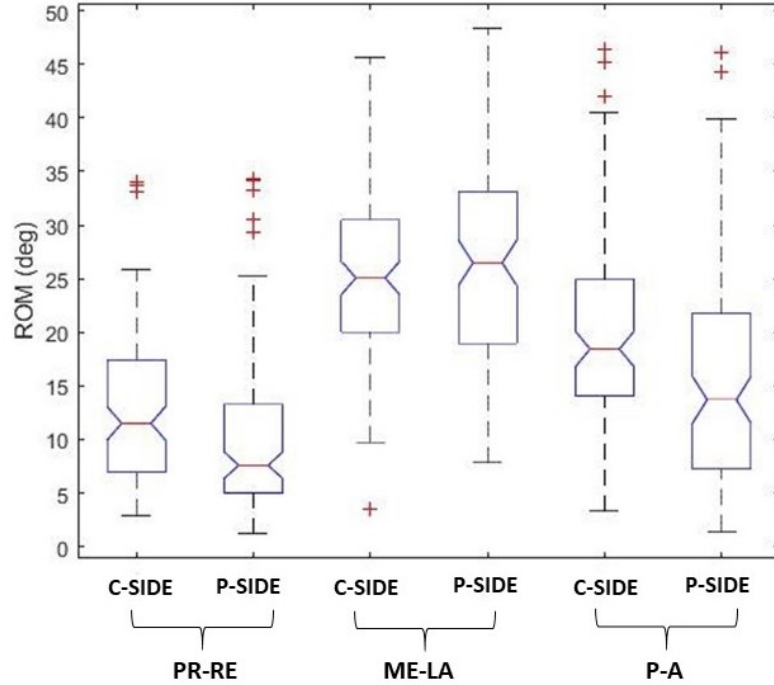


Figure 3.6: ROMs distributions in the sagittal plan for each scapula rotation.

PR-RE		ME-LA		P-A	
Contralateral	Pathological	Contralateral	Pathological	Contralateral	Pathological
p=0.2	p=0.07	p=0.5	p=0.5	p=0.2	p<0.05

Table 3.5: Results of the Lilliefors test on the ROMs distributions.

of humerus elevation (AB-AD). In this case the results of the Lilliefors test are summarized in Table 3.5. Moreover, performing Student's t test it has emerged that no statistically significant differences were found comparing the ROMs distributions of the pathological limb and of the contralateral one, both for the PR-RE ($p = 0.4$) and ME-LA ($p = 0.4$). On the other hand, different results were obtained for posterior-anterior tilting: the Mann-Whitney test highlighted statistically significant differences ($p < 0.05$) between the ROMs distributions of the pathological side and of the contralateral side. In Figure 3.7 the box plots of ROMs distributions in the frontal plan (for each scapula rotation) are shown.

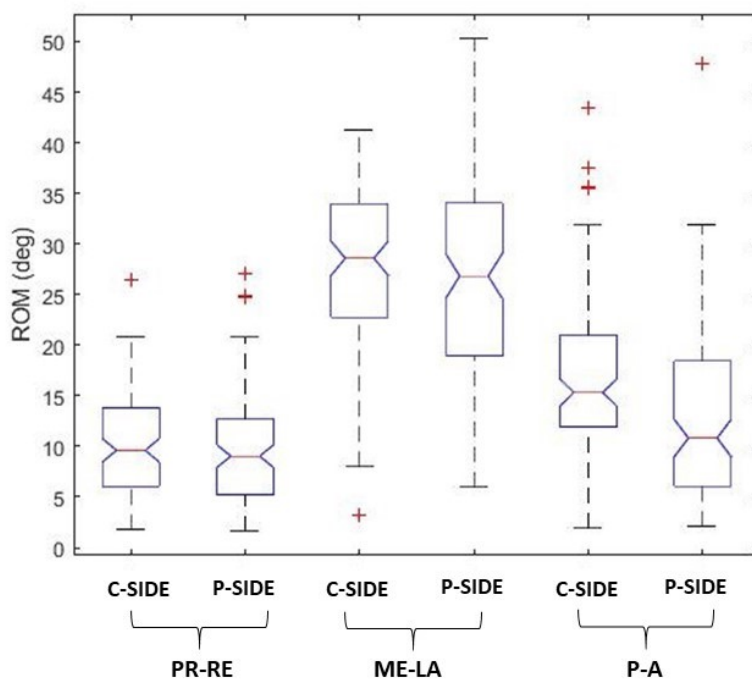


Figure 3.7: ROMs distributions in the frontal plan for each scapula rotation.

3.3 Scapulo-Humeral Rhythm

As described in Section 2.7, for each patient the mean curve (for each angle-angle plot) over the five movement repetitions was obtained and a humerus elevation (and lowering) range between 0° and 120° was considered. This latter was then divided into three equal phases, that are:

1. I_1 between 0° and 40° ;
2. I_2 between 40° and 80° ;
3. I_3 between 80° and 120° .

Performing a linear regression on each of the three segments, the SHR values, which correspond to the slope of the fit line, were obtained.

Considering the scapula PR-RE, Figure 3.8 shows the SHR distributions for the first phase (I_1) of humerus elevation and lowering in the sagittal plan through box plots.

In Figure 3.8, it is possible to note that the four distributions appear to be symmetric with respect to their SHR median values and this could mean that

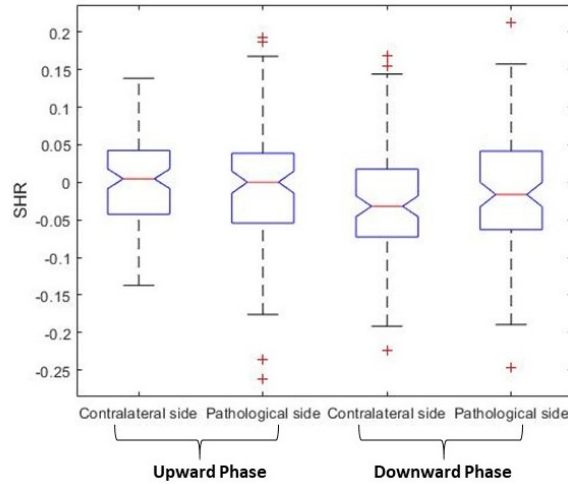


Figure 3.8: PR-RE SHR distributions for the first phase ($I1$) of humerus elevation and lowering in the sagittal plan.

Scapula rotations		I1		I2		I3	
		contralateral limb	pathological limb	contralateral limb	pathological limb	contralateral limb	pathological limb
PR-RE	upward	p=0.1	p=0.5	p<0.05	p=0.3	p=0.5	p=0.1
	downward	p=0.5	p=0.5	p=0.2	p<0.05	p=0.3	p<0.05
ME-LA	upward	p=0.2	p<0.05	p=0.07	p<0.05	p<0.05	p=0.05
	downward	p=0.2	p=0.2	p<0.05	p=0.1	p=0.3	p=0.5
P-A	upward	p=0.5	p=0.3	p=0.5	p=0.2	p=0.1	p=0.2
	downward	p=0.4	p=0.4	p=0.4	p=0.5	p=0.09	p<0.05

Table 3.6: Lilliefors test results (sagittal plan).

SHR are normally distributed. For that reason, the assumption of normality, for the SHR distributions over the three phases of humerus elevation and lowering (in the sagittal plan) for each scapula rotation, was checked through Lilliefors test. The results are shown in Table 3.6.

Based on these results, it was chosen whether to apply Mann-Whitney test or Student's t test to compare SHR distributions of the contralateral and pathological side. The results are summarized in the Table 3.7, where it was reported with an asterisk (*) when Mann-Whitney test was performed.

Table 3.7 highlights the fact that, with regard to medio-lateral rotation, the SHR distributions of the contralateral and pathological limb differ in the first two intervals of the upward phase and in the last two of the downward phase. Statistically significant differences are also present in the first interval of the

Scapula rotations		I1	I2	I3
PR-RE	upward	p=0.6	p=0.9*	p=0.8
	downward	p=0.3	p=0.2*	p=0.8*
ME-LA	upward	p<0.05*	p<0.05*	p=0.3*
	downward	p=0.9	p<0.05*	p<0.05
P-A	upward	p=0.8	p=0.6	p=0.5
	downward	p<0.05	p=0.2	p=0.5*

Table 3.7: Results of the comparison between the SHR distributions of the contralateral and pathological limb (sagittal plan).

Scapula rotations		I1		I2		I3	
		contralateral limb	pathological limb	contralateral limb	pathological limb	contralateral limb	pathological limb
PR-RE	upward	p=0.09	p=0.5	p=0.3	p=0.2	p=0.5	p=0.3
	downward	p=0.4	p<0.05	p=0.5	p<0.05	p=0.3	p=0.5
ME-LA	upward	p=0.5	p=0.4	p=0.1	p<0.05	p=0.5	p=0.3
	downward	p=0.09	p<0.05	p=0.5	p=0.5	p=0.2	p=0.5
P-A	upward	p<0.05	p=0.3	p=0.3	p=0.5	p=0.4	p=0.5
	downward	p<0.05	p<0.05	p=0.5	p=0.5	p=0.3	p=0.4

Table 3.8: Lilliefors test results (frontal plan).

downward phase in the posterior-anterior tilting.

The same steps were followed to carry out the analysis in the frontal plan. In particular, considering the scapula ME-LA, Figure 3.9 shows the SHR distributions for the first phase (I1) of humerus elevation and lowering in the frontal plan.

Figure 3.9 highlights the fact that, concerning downward phase, the SHR values of the pathological side doesn't seem to follow a Gaussian distribution. The assumption of normality, for the SHR distributions over the three phases of humerus elevation and lowering (in the frontal plan) for each scapula rotation, was then checked through Lilliefors test. The results are shown in Table 3.8.

Based on these results, it was chosen whether to apply Mann-Whitney test or Student's t test to compare SHR distributions of the contralateral and pathological side. The results are summarized in the Table 3.9, where it was reported with an asterisk (*) when Mann-Whitney test was performed.

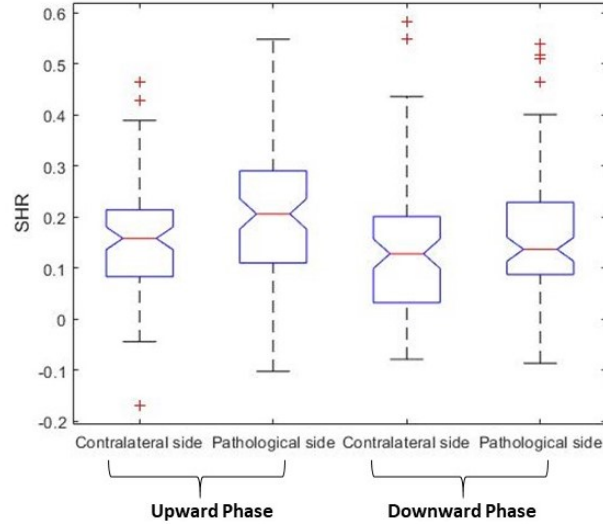


Figure 3.9: ME-LA SHR distributions for the first phase ($I1$) of humerus elevation and lowering in the frontal plan.

Concerning the medio-lateral rotation in the frontal plan, again the SHR distributions of the contralateral and pathological limb differ in the first two intervals of the upward phase and in the last two of the downward phase. It is also possible to note that statistically significant differences are present in the first and in the last interval of the upward phase and in the last interval of the downward phase in the protraction-retraction. Moreover, the SHR distributions of the contralateral and pathological limb differ in the second interval of the upward phase of the posterior-anterior tilting.

3.4 Prediction bands

As described in Section 2.8, prediction bands (based on the Gaussian theory) have been calculated in order to describe the contralateral-to-pathological side differences in the scapulo-humeral coordination of patients.

Figures 3.10, 3.11 and 3.12 report the prediction bands, respectively for scapula protraction-retraction, medio-lateral rotation and posterior-anterior tilting, considering the humerus elevation in the sagittal plan. Comparison of prediction bands (PBs) for contralateral and pathological upper limb is show in each angle-angle plot. For each side three lines are reported: the central is the mean curve

Scapula rotations		I1	I2	I3
PR-RE	upward	$p < 0.05$	$p = 0.5$	$p < 0.05$
	downward	$p = 0.1^*$	$p = 0.9^*$	$p < 0.05$
ME-LA	upward	$p < 0.05$	$p < 0.05^*$	$p = 0.08$
	downward	$p = 0.2^*$	$p < 0.05$	$p < 0.05$
P-A	upward	$p = 0.3^*$	$p < 0.05$	$p = 0.6$
	downward	$p = 0.3^*$	$p = 0.1$	$p = 0.7$

Table 3.9: Results of the comparison between the SHR distributions of the contralateral and pathological limb (frontal plan).

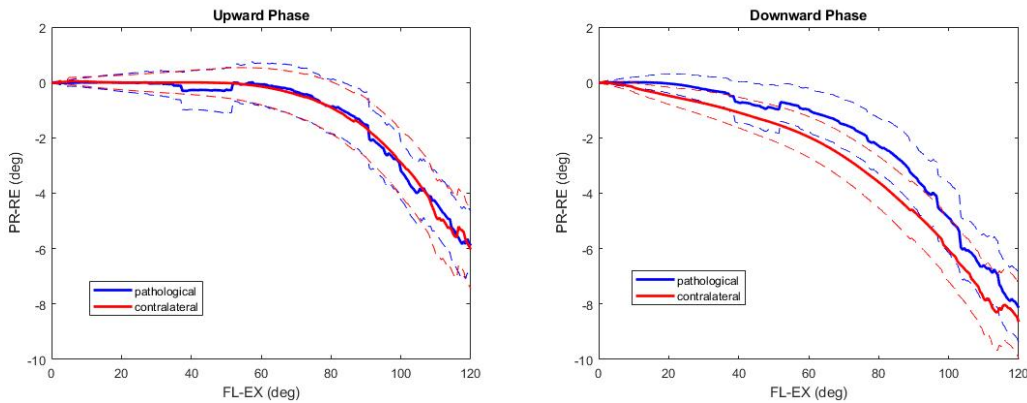


Figure 3.10: Scapula PR-RE: comparison of contralateral and pathological PBs for the upward and downward phase of humerus elevation in the sagittal plan.

calculated over all patients, while the other two (dotted lines) are the upper and the lower prediction bands. These latter are obtained by considering point-by-point intervals with amplitude 1.96 either side of the mean, that is the 95% confidence interval.

Concerning Figures 3.10 and 3.12, it is possible to note that the PBs of the upward phase are almost overlapping. On the other hand, Figure 3.11 shows two distinct PBs for the pathological and contralateral limb in the upward phase. Considering, instead, the prediction bands of the downward phases it emerges that:

- in Figure 3.10 the mean curve of the contralateral side overlaps with the

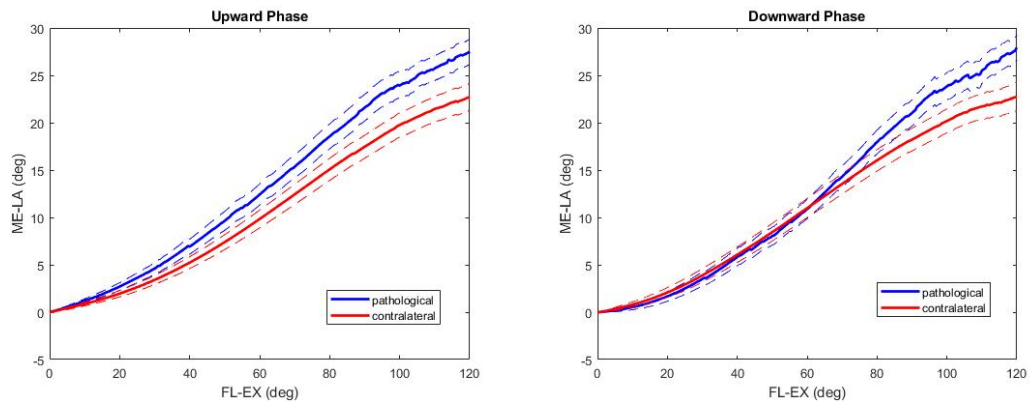


Figure 3.11: Scapula ME-LA: comparison of contralateral and pathological PBs for the upward and downward phase of humerus elevation in the sagittal plan.

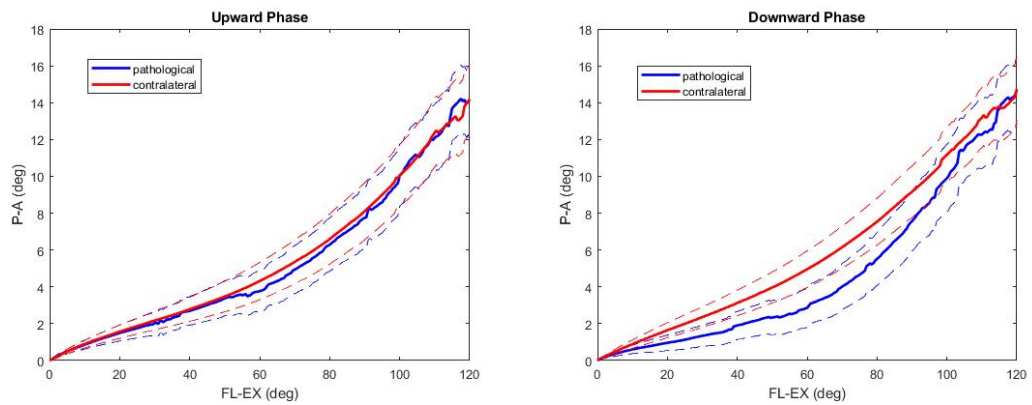


Figure 3.12: Scapula P-A: comparison of contralateral and pathological PBs for the upward and downward phase of humerus elevation in the sagittal plan.

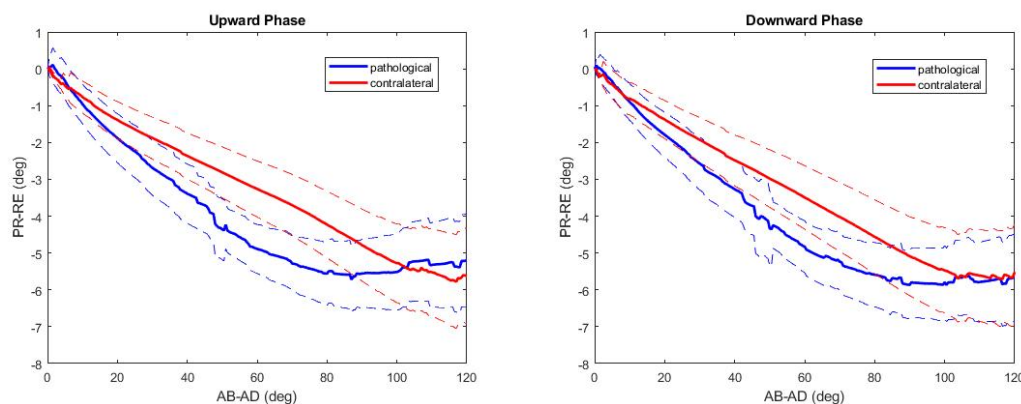


Figure 3.13: Scapula PR-RE: comparison of contralateral and pathological PBs for the upward and downward phase of humerus elevation in the frontal plan.

lower limit of the pathological side PB and the mean curve of the pathological limb overlaps with the upper limit of the contralateral limb PB;

- in Figure 3.11 the PBs are almost overlapping until about 70° of humerus elevation, then the two bands become distinct;
- Figure 3.12 shows two distinct PBs for the pathological and contralateral limb until about 70° of humerus elevation.

Figures 3.13, 3.14 and 3.15 report the prediction bands, respectively for scapula PR-RE, ME-LA and P-A, considering the humerus elevation in the frontal plan. Again, for each side (pathological and contralateral) three lines are reported: the central is the mean curve calculated over all patients, while the other two (dotted lines) are the upper and the lower prediction bands.

In Figure 3.13 it is possible to note that the two PBs of the upward phase seem to be separate between 50° and 70° of humerus elevation, while overlapping between 90° and 120° . It is also possible to find this overlap in the angle-angle plot of the downward phase, while between 10° and 40° of humerus elevation the mean curve of the contralateral side overlaps with the upper limit of the pathological PB and the mean curve of the pathological side overlaps with the lower limit of the contralateral PB.

In Figure 3.14 the PBs seem to be distinct in the upward phase, although the lower limit of the pathological PB and the upper limit of the contralateral PB are overlapping. Concerning the downward phase, it is possible to note that, until about 90° of humerus elevation, the mean curve of the contralateral side

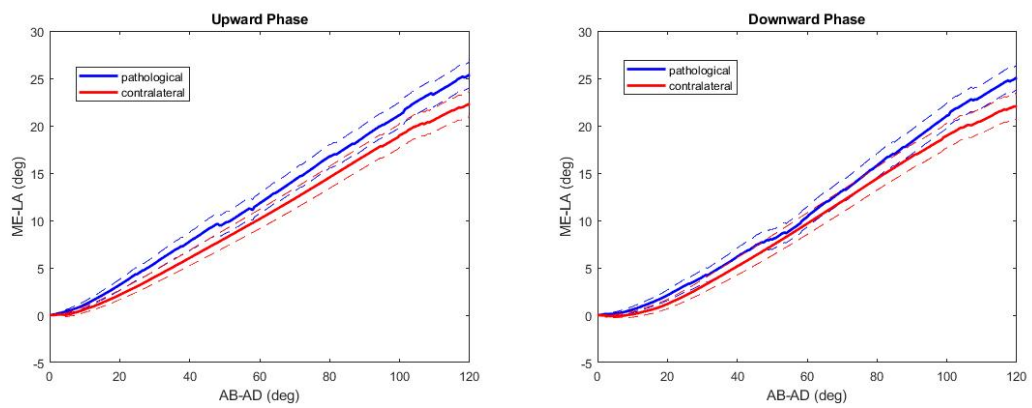


Figure 3.14: Scapula ME-LA: comparison of contralateral and pathological PBs for the upward and downward phase of humerus elevation in the frontal plan.

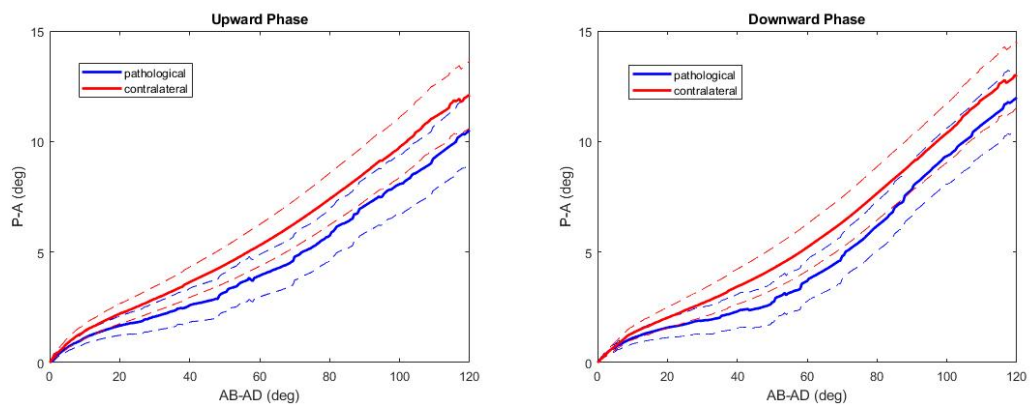


Figure 3.15: Scapula P-A: comparison of contralateral and pathological PBs for the upward and downward phase of humerus elevation in the frontal plan.

overlaps with the lower limit of the pathological side PB and the mean curve of the pathological limb overlaps with the upper limit of the contralateral limb PB. After 90° of humerus elevation the two bands become distinct.

Figure 3.15 highlights that the mean curve of the contralateral side overlaps with the upper limit of the pathological PB and the mean curve of the pathological side overlaps with the lower limit of the contralateral PB, both for the upward and downward phase.

Chapter 4

Discussion and Conclusions

A clinical parameter heavily affected in most shoulder disorders is the scapulo-humeral rhythm (SHR) [2], which is the coordinate movement between scapula and humerus, when the latter is elevated. Several methods have been developed to measure the SHR, which can be differentiated based on the scapular tracking technique. A recent, non-invasive and easy to use technique is the one proposed by Cutti et al. [13], as part of the "INAIL Shoulder & Elbow Outpatient protocol" (ISEO), which is based on inertial and magnetic sensors: the tracking of the scapula is performed using a sensor positioned directly on the skin, just above the scapular spine [15]. Preliminary results have confirmed the validity of ISEO to measure upper-limb kinematics [13],[15].

In this thesis project, a group of 108 patients with a diagnosis of full thickness rotator cuff tears (which represents one of the most common shoulder pathology in the working population [4],[5]) was considered and the upper limb kinematics of the patients was assessed with ISEO, using *WISE* inertial and magnetic sensors, in order to extrapolate the parameters of clinical interest.

First of all, the repeatability of the movement has been taken into account and for each patient the coefficient of multiple correlation has been evaluated. Results for CMC showed that no significant are present on the CMC distributions of the PR-RE upward and downward phases for the contralateral side. The same results were obtained for the pathological side and for the ME-LA and P-A upward and downward phases. Moreover, in Tables 3.1, 3.2, 3.3 and 3.4 the CMC percentages are summarized. From these latter, it emerges that the medio-lateral rotation in the sagittal plan is characterized by an excellent CMC both for the contralateral and pathological side: it results > 0.95 in 82% and

70% of cases respectively. It is also true for the frontal plan where the CMC results > 0.95 in 80% of cases for the contralateral limb and in 69% of cases for the pathological limb. It is possible to note, however, lower percentages for both the protraction-retraction and the posterior-anterior tilting, considering the sagittal and the frontal plan. Concerning the protraction-retraction, a possible cause could be linked to an instrumental factor. In fact, it is known that the PR-RE angles are the ones that the sensors estimate with more difficulty and this could be reflected in a less accurate acquisition of the joint movement, resulting in a lower CMC. Another possible factor influencing these percentages could be related to the pathology of patients analysed. As mentioned above, in this study are involved patients with a diagnosis of full thickness rotator cuff tears at a pre-operative stage. The presence of pain and compensatory movements (which also affect the contralateral side) could play a key role in the repeatability of the movement. Therefore, it might be interesting to check out how these percentages change during the longitudinal study, which involves analysing patients at 3, 6 and 12 months after the operation. Therefore, it was chosen not to exclude any patient and to extrapolate the clinical parameters of interest (that are, ranges of motion and scapulo-humeral rhythm) even for subjects with a very low CMC (< 0.55), so they could be compared to those obtained at each follow up.

The humerus and scapula ranges of motion have been then calculated and analysed in order to verify the existence of statistically significant differences in their distributions, related to the pathology.

In general, statistically significant differences have been found between the ROMs distributions of the pathological and contralateral limb, except for the medio-lateral rotation in the sagittal and frontal plan and the protraction-retraction in the frontal plan (Figures 3.6 and 3.7). In addition, the ROMs median values for the pathological limb were found to be lower than those of the contralateral limb.

Another parameter of clinical interest is certainly the scapulo-humeral rhythm and it has been extrapolated for each patient, following the procedure proposed in [19] and [20]. Again, the contralateral and the pathological limb have been compared in order to evaluate the presence of statistically significant differences between the SHR distributions. It emerged that, with regard to medio-lateral rotation in the sagittal plan, the SHR distributions of the contralateral and pathological limb differ in the first two intervals of the upward phase and in

the last two of the downward phase. Statistically significant differences are also present in the first interval of the downward phase in the posterior-anterior tilting in the sagittal plan. Considering, instead, the ME-LA in the frontal plan, the SHR distributions of the contralateral and pathological limb differ in the first two intervals of the upward phase and in the last two of the downward phase. In addition, statistically significant differences are present in the following intervals:

- in the first and in the last interval of the upward phase in PR-RE;
- in the last interval of the downward phase in PR-RE;
- in the second interval of the upward phase in P-A.

These results are summarized in Tables 3.7 and 3.9.

It will be interesting to compare these results, both in terms of ranges of motion and scapulo-humeral rhythm, with those obtained at each follow up, in order to evaluate the recovery of patients, after the surgical and rehabilitative treatments. In addition, the importance of acquiring both the pathological and the contralateral limb lies in the fact that for the patients involved in this study, the contralateral side is usually considered as reference.

Lastly, the prediction bands (based on the Gaussian theory) have been computed in order to describe the contralateral-to-pathological side differences in the scapulo-humeral coordination of patients. The relevance of this side-to-side analysis is linked to the possibility of within-patient evaluation. In addition, these PBs have been calculated both for the upward and downward phase of humerus elevation because they are characteristic of different kinematic patterns.

It is possible to note that, concerning the upward phase of the humerus elevation in the sagittal plan, the medio-lateral rotation PBs and the posterior anterior tilting PBs of the contralateral and pathological limb are completely overlapping. On the other hand, Figure 3.11 shows two distinct ME-LA PBs for the pathological and contralateral limb in the upward phase of humerus elevation in the sagittal plan. The same pattern is shown in Figure 3.14 for the frontal plan: the PBs seem to be distinct in the ME-LA upward phase, although the lower limit of the pathological PB and the upper limit of the contralateral PB are overlapping.

Furthermore, in order to achieve a more complete characterization of the kinematic patterns that describe patients affected by full thickness rotator cuff tears, it could be significant to compare the prediction bands computed in this study to those obtained from a group of healthy subjects.

Bibliography

- [1] Kapandji I.A. *Fisiologia articolare*. 2010. Mailone. Monduzzi Editore;
- [2] Ludewig PM, Reynolds JF. The Association of Scapular Kinematics and Glenohumeral Joint Pathologies. *J Orthop Sports Phys Ther* 2009; 39(2):90-104;
- [3] Nordin M. and Frankel V.H., *Basic Biomechanics of Musculoskeletal System*. 1989. Lea & Febiger, Philadelphia, London;
- [4] Mell A.G., LaScalza S., Guffey P., Ray J., Maciejewski M., Carpenter J.E., Hughes R.E., Arbor A. Effect of rotator cuff pathology on shoulder rhythm. *J Shoulder Elbow Surg* 2005. 14:58S64S;
- [5] Seo S.S., Choi J.S., An K.C., Kim J.H., Kim S.B. The factors affecting stiffness occurring with rotator cuff tear. *J Shoulder Elbow Surg* 2012. 21: 304-309;
- [6] Ludewig PM, Reynolds JF. The Association of Scapular Kinematics and Glenohumeral Joint Pathologies. *J Orthop Sports Phys Ther* 2009; 39(2): 90-104;
- [7] De Baets L., Jaspers E., Desloovere K., Van Deun S. A systematic review of 3D scapular kinematics and muscle activity during elevation in stroke subjects and controls. *J Electromyogr Kinesiol*;
- [8] Sabatini A.M., Estimating Three-Dimensional Orientation of Human Body Parts by Inertial/Magnetic Sensing. *Sensors* 2011, 11, 1489-1525;
- [9] Valenti R.G., Dryanovski I. and Xiao J., Keeping a Good Attitude: A Quaternion-Based Orientation Filter for IMUs and MARGs. *Sensors* 2015, 15, 19302-19330;

- [10] MEMSIC, Inc - Magnetic Sensor Components — MMC3416xPJ Available online: <http://www.memsic.com/magnetic-sensors/MMC3416xPJ> (accessed on Nov 12, 2018);
- [11] LIS344ALH - 3-axis analog accelerometer, ± 2 g / ± 6 g user selectable full-scale, ultra compact, low power - STMicroelectronics Available online: <https://www.st.com/en/mems-and-sensors/lis344alh.html> (accessed on Oct 3, 2019);
- [12] FXAS21002 — 3-Axis Digital Gyroscope — NXP Available online: <https://www.nxp.com/products/no-longer-manufactured/3-axis-digital-gyroscope:FXAS21002C> (accessed on Oct 3, 2019);
- [13] Cutti A.G., Giovanardi A., Rocchi L., Davalli A., Sacchetti R. Ambulatory measurement of shoulder and elbow kinematics through inertial and magnetic sensors. *Med Bio Eng Comput* 2008; 46(2): 169-78;
- [14] Borstad JD, Ludewig PM. Comparison of scapular kinematics between elevation and lowering of the arm in the scapular plane. *Clin Biomech* 2002; 17(9-10): 650-9;
- [15] Parel I., Cutti A.G., Fiumana G., Porcellini G., Verni G., Accardo A.P. Ambulatory measurements of the scapulohumeral rhythm: intra- and inter operator agreement of a protocol based on inertial and magnetic sensors. *Gait & Posture* 2012, 35:636-640;
- [16] Kadaba M.P., Ramakrishnan H.K., Wootten E., Gainey J., Gorton G., Cochran G.V.B. Repeatability and electromiographic data in normal adult gait. *J Orthop Res* 1989; 7: 849-860;
- [17] Press W.H., Teukolsky S.A., Vetterling W.T. and Flannery B.P., *Numerical Recipes. The Art of Scientific Computing. Third Edition*;
- [18] Martin B.R., *Statistics For Physical Sciences. An Introduction*;
- [19] Mell A.G., LaScalza S., Guffey P., Ray J., Maciejewski M., Carpenter J.E., Hughes R.E. and Arbor A. Effect of rotator cuff pathology on shoulder rhythm. *Journal of Shoulder Elbow Surgery* 2005;

- [20] Scibek J.S., Mell A.G., Downie B.K., Carpenter J.E., Hughes R.E. and Arbor A. Shoulder kinematics in patients with full-thickness rotator cuff tears after subacromial injection. *Journal of Shoulder Elbow Surgery* 2008;
- [21] Parel I., Cutti A.G., Fiumana G., Porcellini G., Verni G., Accardo AP. Changes in the scapulohumeral rhythm of patients treated arthroscopically for rotator-cuff tear over a period of 90 days. *Proceeding at ISB XXII*, Brussels, Belgium, 2011.
- [22] Cutti A.G., Parel I., Raggi M., Petracci E., Pellegrina A., Porcellini G., Accardo A.P. and Verni G. Prediction bands and intervals for the scapulohumeral coordination based on Bootstrap and Gaussian theories. *Gait & Posture*;
- [23] Duhamel A., Bourriez J.L., Devos P., Krystkowiak P., DestÃ©e A., Derambure P., Defebvre L. Statistical tools for clinical gait analysis. *Gait & Posture*. 2004 Oct;20(2):204-12.

Ringraziamenti

Alla fine di questo percorso desidero fortemente ringraziare tutti coloro che ne hanno preso parte e che hanno contribuito alla realizzazione di questo elaborato. In primo luogo vorrei ringraziare il professor Nico Lanconelli, per i preziosi consigli che mi ha fornito durante lo svolgimento del lavoro.

Vorrei, inoltre, ringraziare l'Ing. Marco Muraccini per la fiducia che mi ha dimostrato fin dall'inizio di questo progetto e per avermi seguita durante tutti questi mesi di lavoro.

Grazie ad Antonella, compagna fedele di trasferte, per avermi supportata in questo cammino.

Grazie all'Ing. Matteo Mantovani per avermi accolta presso l'azienda NCS Lab di Carpi e al suo staff per la cordialità e disponibilità dimostratami.

Desidero infine ringraziare il Dr. Claudio Chillemi e tutti gli specializzandi dell'ICOT di Latina.